

INVESTIGATION OF DIFFERENT HATCH STRATEGIES ON
HIGH ENTROPY ALLOY FABRICATION
BY SELECTIVE LASER MELTING

A Thesis
by
JONI CHANDRA DHAR

Submitted to the Graduate College of
The University of Texas Rio Grande Valley
In partial fulfillment of the requirements for the degree of

MASTER OF SCIENCE IN ENGINEERING

August 2021

Major Subject: Manufacturing Engineering

INVESTIGATION OF DIFFERENT HATCH STRATEGIES ON
HIGH ENTROPY ALLOY FABRICATION
BY SELECTIVE LASER MELTING

A Thesis
by
JONI CHANDRA DHAR

COMMITTEE MEMBERS

Dr. Jianzhi Li
Chair of Committee

Dr. Rajiv Nambiar
Committee Member

Dr. Richard Crawford
Committee Member

Dr. Mohammed Uddin
Committee Member

August 2021

Copyright 2021 Joni Chandra Dhar

All Rights Reserved

ABSTRACT

Dhar, Joni Chandra, Investigation of Different Hatch Strategies on High Entropy Alloy Fabrication by Selective Laser Melting. Master of Science in Engineering (MSE), August, 2021, 68 pp., 11 Tables, 23 Figures, 87 References.

This study investigated the synthesis of CuCrFeNiTiAl high entropy alloy (HEA) from pure elements using selective laser melting (SLM). The objectives are to validate the feasibility of the HEA fabrication from elemental powder materials, and to examine the effect of various hatch strategies and energy densities on the microstructures and other materials properties. 3D samples of CuCrFeNiTiAl alloy were fabricated under different energy densities and with different scan vector lengths. The as-built samples were characterized by X-ray diffraction (XRD), and the microstructures were observed using scanning electron microscopy (SEM). The XRD results showed that face centered cubic, and body centered cubic structures were mostly present in all samples. Analysis of SEM pictures revealed that laser energy density has a correlation with size, shape and area of grains formed. Four types of grain microstructures observed from SEM pictures are dendrites, rosette, petals, and branches type structures. The morphologies of the grain structures were greatly affected by laser scan vector length. Shorter scan vectors facilitated development of more dendritic structures, and larger grains. As the number of grains decreased due to shorter scan lengths, the micro-hardness of the as-built samples were also reduced. Moreover, shorter scan vectors improved the surface quality of the printed samples.

DEDICATION

I dedicate my work to my mother, Arpana Rani Dhar; my father, Babul Chandra Dhar; and my four elder sisters. Thanks to the almighty for helping me and guiding me through the difficult times. Without the constant support and help of my supervisor, family and friends, my journey here at UTRGV would not have been possible.

ACKNOWLEDGMENT

I would like to acknowledge my supervisor, Dr. Jianzhi Li, for his outstanding guidance and support. His knowledge and expertise in the additive manufacturing field and his ongoing mentorship have helped me overcome all the difficulties I faced during this master's program. I am delighted that I got the opportunity to work in the Advanced Manufacturing Lab under his supervision. Besides, I am very thankful to Dr. Shanshan Zhang, Dr. Ben Xu, and Dr. Farid Ahmed. I would specially mention Dr. Shanshan Zhang as her continuous learning mentality, and industriousness motivated me a lot. I have learned a lot from Dr. Shanshan Zhang, as she has excellent experience in additive manufacturing. I want to thank Al Mazedur Rahman, Shofe Ahmed Mazumder, Provashish Roy, and Md. Rafat for making my journey smooth at the earlier stage. I am also thankful to my colleagues Lazaro Lopez Mendez, Sheddar Escalante for their continuous encouragement and support.

TABLE OF CONTENTS

	Page
ABSTRACT.....	iii
DEDICATION.....	iv
ACKNOWLEDGMENT.....	v
TABLE OF CONTENTS.....	vi
LIST OF TABLES.....	ix
LIST OF FIGURES	x
CHAPTER I. INTRODUCTION.....	1
1.1 High-Entropy Alloy	1
1.2 Core Effects of HEA.....	2
1.2.1 High-entropy effect.....	3
1.2.2 Severe Lattice Distortion	3
1.2.3 Sluggish Diffusion	4
1.2.4 Cocktail Effect	5
1.3 Problem Statement.....	5
1.4 Research Objectives.....	6

1.5 Thesis Organization	7
CHAPTER II. LITERATURE REVIEW	8
2.1 Crystal Structure of HEA.....	8
2.2 Microstructural Morphology of HEA	10
2.3 Mechanical Properties.....	11
2.3.1 Wear Behavior	11
2.3.2 Fatigue Behavior.....	12
2.3.3 Corrosion Properties	13
2.3.4 High Temperature Properties.....	13
2.4 Selective Laser Melting & Processing Parameters	14
2.4.1 Laser Scanning Strategy	15
2.4.2 Scanning Direction.....	16
2.4.3 Hatch Spacing	18
2.4.4 Scan Vector Length.....	18
CHAPTER III. METHODOLOGY	20
3.1 Materials	20
3.2 Powder Mixing.....	21
3.3 AM Fabrication.....	22
3.3.1 5X5 Test Series of CuCrFeNiTiAl HEA	22
3.3.2 3X3 Test Series of CuCrFeNiTiAl & CuCrFeNiTi HEA	24

3.4 Testing Method	27
CHAPTER IV. RESULT AND DISCUSSION	29
4.1 XRD Analysis	30
4.2 Microstructure analysis.....	32
4.2.1 5X5 test series samples	32
4.2.2 2Y and 2Z samples with Al	34
4.2.3 Sample 2Z _{1.5} Vs Sample 2Z _{0.5}	34
4.2.4 Sample 2Y Vs Sample 2Z.....	39
4.2.5 2Z Samples Without Al	41
4.3 EDX Element Analysis	44
4.3.1 Sample 1A, 2B, and 3C of CuCrFeNiTiAl HEA.....	44
4.3.2 Sample 2Y and 2Z of CuCrFeNiTiAl HEA.....	46
4.3.3 Sample 2Y and 2Z of CuCrFeNiTi HEA.....	50
4.4 Micro hardness of HEA Samples.....	51
4.5 Surface Roughness of HEA Builds.....	53
CHAPTER V. CONCLUSION.....	59
REFERENCES	62
BIOGRAPHICAL SKETCH	68

LIST OF TABLES

	Page
Table 1: Physical properties and details of elemental metal powders	21
Table 2: Powder mixing protocol of CuCrFeNiTiAl alloy system.....	21
Table 3: Powder mixing protocol of CuCrFeNiTi alloy system.....	21
Table 4: 5X5 test series design	23
Table 5: Energy density (J/mm ²) of 5X5 Test Series.....	23
Table 6: Parameter settings for 3X3 test series according to Taguchi design	25
Table 7: Chemical composition of CuCrFeTiNiAl2.5 alloys in bright and dark areas.	46
Table 8: EDS of both samples	50
Table 9: Mixing enthalpy of binary equiatomic alloys calculated by Miedema approach.....	51
Table 10: Micro-hardness of as-built CuCrFeNiTiAl and CuCrFeNiTi HEAs.....	51
Table 11: Surface roughness of as-built CuCrFeNiTiAl and CuCrFeNiTi HEAs.....	55

LIST OF FIGURES

	Page
Figure 1: SEM pictures of raw metal powders (A) Cu, (B) Cr, (C) Fe, (D) Ni, (E) Ti, and (F) Al.....	20
Figure 2: (a) Detailed dimension 5X5 of the test series (b) SLM printed part	24
Figure 3: Detailed dimension of 3X3 test series.....	26
Figure 4: SLM printed 3X3 test series.....	26
Figure 5: Specimens printed for surface roughness and micro-hardness measurement	28
Figure 6: Pictures of 3X3 test series samples after laser melting process of CuCrFeNiTi HEA	30
Figure 7: XRD patterns of CuCrFeNiTiAl HEA samples under different energy densities (LEDA, MEDA, & HEDA) and of CuCrFeNiTi HEA samples (2Y & 2Z).....	31
Figure 8: SEM pictures of CuCrFeNiTiAl sample of (a) 1A at low magnification; and samples of (b) 1A, (c) 3C, and (d) 5E at high magnification.....	33
Figure 9: Surface of as built 2Z samples (with Al) with (A) 1.5 mm (B) 1 mm (C) 0.75 mm and (D) 0.5mm scan vectors	35
Figure 10: (A) Low magnification picture of 2Z _{1.5} sample, (B) rosette (C) dendritic, (D), (E), (F) petals, & (G), (H) branches structures	37

Figure 11: (A) Low magnification picture of 2Z _{0.5} sample, (B) petals (C), (D), (E) dendrites (F) & (G) petals with rosette (H) small petal structures	38
Figure 12: Microstructures in the stripe areas of samples (A) & (B) 2Y _{1.5} , (C) &(D) 2Z _{1.5}	39
Figure 13: (A) & (B) Low magnification picture of 2Y _{1.5} sample, (C) & (D) petals, branches, and dendrites, (E) dendrites, (F) rosette structures with petals.....	41
Figure 14: (A) low magnification picture of sample 2Z _{1.5} (B) & (C) melt pool and overlapping area interface, (D) small petals in melt pool area, (E) petals in overlapping, (F) dendritic structure	42
Figure 15: (A) & (B) low magnification pictures of sample 2Z _{0.5} , (C) petal and dendrites, (D) & (E) dendrites, (F) dendrites with rosette structures	43
Figure 16. Chemical composition of (a) bright area and (b) dark area of CuCrFeNiTiAl samples.....	44
Figure 17: EDS mapping pictures of CuCrFeNiAl HEA in sample 2Y. (A) low magnification picture of sample surface, (B) distribution of all elements, & (C) individual element's distributions	47
Figure 18: EDS mapping pictures of CuCrFeNiAl HEA in sample 2Z. (A) low magnification picture of sample surface, (B) distribution of all elements, & (C) individual element's distributions	48
Figure 19: EDS mapping pictures of CuCrFeNiAl HEA in sample 2Y. (A) higher magnification picture of sample surface in dendritic area, (B) distribution of all elements, & (C) individual element's distributions.....	49

Figure 20: Average micro hardness of different CuCrFeNiTiAl HEA samples.....	52
Figure 21: Mahr GombH M300C surface roughness testing device	54
Figure 22: Average surface roughness of different CuCrFeNiTiAl HEA samples	55
Figure 23: Surface roughness testing specimens of samples (A) 2Y0.5, (B) 2Y1.5, (C) 2Z0.5 & (D) 2Z1.5.....	57

CHAPTER I

INTRODUCTION

New material development is very important in materials science, especially due to the limited resources and increased public demand. Conventional alloys have only one or two major elements, and very small amounts of other elements are mixed which cannot improve the properties of major elements significantly. As a new class of material, high-entropy alloys (HEA) have brought a revolution in alloy design and have showed a great potential of producing multicomponent alloys with supreme properties. This chapter introduces an overview of the high-entropy alloy by discussing core effects of these systems, defines problem statement, describes research objectives, and finally provides outline of the thesis.

1.1 High-Entropy Alloy

High-entropy alloys (HEA) as a new family of alloys are composed of five or more principal elements in equimolar or near-equimolar concentrations [1, 2]. HEAs contain principal elements with concentration between 5 to 35 at %, and minor elements each below 5 at % [2]. By combining multiple elements in an alloy system, HEAs are showing a great possibility for designing novel materials with superior properties expected under extreme operating conditions (high temperature, high pressure, etc.) in many applications in the defense and energy industries such as nuclear reactors, missiles, jet engine, nozzle, turbine blade, compressor blade of aero engine, etc.

The earliest attempts to design HEAs are the research works of two research groups led by Prof. B. Cantor and Prof. J.W. Yeh in 2004 [3, 4]. Both the groups investigated multicomponent alloy systems, which triggered the development of high entropy alloy. Prof. J.W. Yeh is the first who thoroughly described four core effects of high entropy alloys: high-entropy effect, lattice distortion, sluggish diffusion, and cocktail effect [5]. Following these pioneering works, researchers have studied many HEA systems. CuCrFeCoNiAl [6-9] and its Cu free derivations [10, 11] are the most comprehensively studied alloy systems among all the HEA systems reported. One of the important derivatives is CuCrFeNiTiAl where Co is replaced by Ti. As titanium has the highest negative mixing enthalpy with rest of the elements, inclusion of titanium in HEA system causes different intermetallic phases to grow. These phases strengthen HEA with improved strength and hardness [12, 13]. Besides, the solid solution strengthening mechanism of titanium, due to its higher atomic radius, enhances strength of alloys greatly[13]. Therefore, CuCrFeNiTiAl HEA system have a high potential of creating HEAs with promising performance.

1.2 Core Effects of HEA

Although it is expected that multi principal alloys may have several complex phases and intermetallic compounds, many investigations have found HEAs generally maintain simple solid solution phases [14-16]. The formation of intermetallic components is restricted in a high entropy alloy by maximizing the configurational energy of solid solution phase [17]. Four core effects of multi-principal element composition, such as high entropy effect, severe lattice distortion, sluggish diffusion and cocktail effect, as mentioned above, were proposed to explain the observation of random solid solution phase. These effects are discussed below.

1.2.1 High-entropy effect

High-entropy effect tends to stabilize the high-entropy alloy phase. Yeh et al. proposed the ideal case for total free energy of mixing to explain the RSS phase of HEA. The equation for Gibbs free energy of mixing which relates Gibbs free energy with enthalpy (H) and entropy (S) of the mixture is given below:

$$\Delta G_{\text{mix}} = \Delta H_{\text{mix}} - T\Delta S_{\text{mix}} \quad (1)$$

The entropy of the mixture can be calculated using Boltzmann's equation.

$$\Delta S_{\text{mix}} = -R \sum X_i \ln X_i \quad (2)$$

Here, X_i is the concentration of the i^{th} element and R is the gas constant. The total entropy of the HEA system increases with increasing number of elements and the equation (1) gives a lower amount of Gibbs free energy. The less the Gibbs free energy, the more the stability of an alloy. An HEA can be thermodynamically more stable at high temperature since the minimization of Gibbs free energy increases the thermodynamic stability of a material at a constant pressure.

1.2.2 Severe Lattice Distortion

During conventional alloying, solute elements are alloyed in a lattice of solvent element and the atomic misfit among the elements causes strain to develop in the lattice which leads to minor distortion in the lattice. There is no difference between solute and solvent in case of high-entropy alloy as they have equal concentration in the mixture. That is why every lattice site in HEA system have some displacement from the perfect crystal lattice site. Yeh et al. (2007) have conducted a study to investigate the great reduction in the XRD intensities of Cu-Ni-Al-Co-Cr-

Fe-Si alloy system [18]. They systematically continued adding different principal elements with pure copper and thereby they found seven element alloy finally. All the metal combinations were arc melted and then they took their XRD data. They found from the XRD graphs that with increasing number of elements in an alloy system the intensities of peaks in XRD graph decreased drastically under the exact same sample geometry and XRD experimental conditions. In the case of seven element alloy, the main peaks dropped to about the background level. It is due to the severe distortion in the crystal lattice structure which caused fewer Braggs peaks in the XRD graph.

The severity of lattice distortion has been investigated by Pickering et al. (2017) [19]. In their experiment, they measured total scattering in CrMnFeCoNi HEA and compared it with five different derivative alloys of the system with simpler compositions. After analyzing the experimental data, they found that though the lattice distortion in HEA system was greater than that of simpler derivative compositions, the difference was not exceptionally larger.

1.2.3 Sluggish Diffusion

Different constituent elements cause the local lattice fluctuations in the random solid solution phase and the diffusion kinetics is decreased in the HEA system. Due to the disorder of the random solid solution phase, the local lattice potential energy can form deep traps that inhibit diffusion. Tsai et al. (2013) conducted the first ever study to investigate the sluggish diffusion kinetics in a high-entropy alloy system [20]. The diffusion parameters of Co, Cr, Fe, Mn, and Ni in CoCrFeMnNi solid solution were measured using diffusion couple method and compared with different FCC structured metals. The diffusion coefficients were found greater in case of FCC structured metals compared to the CoCrFeMnNi HEA system.

A study to measure the diffusion in a high-entropy system has been conducted by Vaidya, Trubel et al. (2016) [21]. In their study, they used a ^{63}Ni isotope as a tracer to measure diffusion in CoCrFeNi and CoCrFeMnNi alloys at a temperature range of 1073K -1373K by the radiotracer technique. At first, they produced both equiatomic alloys using vacuum arc melting technology and then confirmed their microstructure and phase stability at the given temperature range using X-ray diffraction. Diffusion of Ni in both the alloy systems was found to follow Arrhenius behavior while at a homogeneous temperature, the diffusion was found slow-down with increasing components in the alloy system.

1.2.4 Cocktail Effect

Cocktail Effect is the selection of the specific elements with specific properties that will contribute to the desired properties of the final high-entropy system. An example of this approach is the inclusion of Al and Cr in an alloy to improve the oxidation resistance at high temperature.

1.3 Problem Statement

With the growing interest in research on HEA, many HEA fabrication technologies have been invented such as arc melting, plasma arc sintering, casting, etc. [16, 22-25]. Unlike conventional manufacturing techniques, powder-bed additive manufacturing (AM), such as selective laser melting (SLM) process, has been investigated for HEA fabrication [26, 27]. Studies were reported in literature focusing on the effect of printing parameters (laser power, hatch distance, point distance, exposure time, laser focus diameter, scanning rotation angle, etc.) on the microstructure and properties of alloys made by SLM process [28-30]. However, the reported feedstock of these SLM fabricated HEAs are mostly based on mechanically alloyed

powders [31], which show disadvantages such as high cost, lack of flexibility of material designs, and so on. Up to the date, no reported work is found where HEAs are fabricated from pure elemental metal powders instead of pre-alloyed HEA powder. Therefore, it would be worth investigating the potentiality of HEA fabrication from elemental metal powders.

Usually, during the HEA fabrication by selective laser melting process, laser melts the pre-alloyed HEA powders together and in the final build all the metal elements are found having an elemental distribution as they are pre-alloyed [32-34]. But when elemental powders are used instead of pre-alloyed powders, one of the major challenges in the fabrication process of HEA will be confirming the uniform distribution of all the powders in the mixture. Even all the powders are mixed properly, another major challenge will be ensuring sufficient diffusion among the different metal elements to develop a random solid solution phase. In conventional HEA fabrication processes like arc melting, casting etc., the molten materials get a longer amount of time to cool down and consequently a good diffusion among the elements occurs. However, SLM is a very rapid solidification process where the molten pool doesn't get enough cooling time to ensure the expected diffusion among the elements. Therefore, production of multi-component alloys like HEA with desired elemental ratio by SLM process is a matter of worth investigating.

1.4 Research Objectives

This research aims to investigate the manufacturing of HEA directly elemental powders by selective laser melting. The possibility of HEA production from Cu, Cr, Fe, Ni, Ti powders through selective laser melting will be investigated assuming all the powders are uniformly distributed. In this research, fabrication of HEA is carried out in a Renishaw AM 250 selective laser melting machine at the Metal Additive Manufacturing lab in the University of Texas Rio

Grande Valley. A CuCrFeNiTiAl high entropy alloy system is synthesized directly from elemental powders under different energy densities and laser scanning lengths. Then, the as-built specimens are characterized using X-ray diffraction (XRD) for crystal structures and observed under scanning electron microscopy (SEM). Finally, the micro-hardness and surface roughness of the specimens are measured. The objectives of the research are given below:

1. To verify the feasibility of HEA fabrication from elemental powders via SLM process
2. To examine the effect of different process parameters in SLM, including laser power, exposure time, and point distance, on the microstructures and morphologies of the specimens.
3. To observe the effect of Al addition in the CuCrFeNiTi HEA system.
4. To investigate how the scanning lengths affect the microstructure, mechanical property (micro-hardness), and surface quality of the final build.

1.5 Thesis Organization

This thesis manuscript is organized into five chapters. The first chapter presents the background of the topic of interest, describes the research questions, assumptions, and objectives. The second chapter provides an overview of the HEA system and discusses different research findings in the field of selective laser melting regarding scanning strategy. The full experimental set-up along with the materials processing, parameters settings and testing procedures are described in the third chapter. All the experimental findings are described and discussed in the fourth chapter. Finally, chapter five provides conclusion of the research work.

CHAPTER II

LITERATURE REVIEW

High Entropy Alloys (HEA) are composed of five or more principal constituent elements with equimolar or near-equimolar ratio. The concept of HEA has introduced an excellent way to fabricate advanced materials with superior properties. HEAs have exhibited many attractive properties including superior mechanical properties, excellent wear and fatigue behavior, good resistance to corrosion and shown significant potential for industrial applications. This chapter provides a concise overview on the crystal growth and microstructural properties of different HEA systems with a focus on CuCrFeNiTiAl alloy, reveal their impressive mechanical and other properties, and summarizes the findings from various research works attempted to improve the printing in the selective laser melting additive manufacturing technology.

2.1 Crystal Structure of HEA

X-ray diffraction (XRD) analysis is usually conducted to characterize the development of the alloy microstructure. XRD data gives us information mostly about material crystal structure, and grain size of particles. Common crystalline structures are body centered cubic (bcc), face centered cubic (fcc), hexagonal close packing (hcp) etc. A lot of research has been conducted on the XRD system and currently, most of the research on materials depends on XRD to characterize the material.

Multicomponent alloys may have different phases, like solid solution, intermetallic compounds, amorphous phase. Solid solution found on HEAs are normally fcc, bcc or mixed of both structures. The mechanical energy of a HEA depends on the crystal structures. Fcc structures are quite ductile but their strengths are relatively low. On the other hand, bcc structures are brittle, but much harder. So, crystal structure is very crucial in HEA design [35]. While many literatures reported single fcc phase [36-38] solid solution and single bcc phase solid solution[39-41] found in HEAs, single hcp phase [42-44] multicomponent alloys were also found in a few investigations.

Many studies have been done on HEA systems with changing percentages of Aluminum. Yeh et al. (2004) have investigated as-cast CuCoNiCrFeAl_x high-entropy alloy system where the values of x are from 0 to 3 [4]. They found a simple fcc structure for aluminum contents from x=0 to x= 0.8. A bcc structure appeared with fcc structure for aluminum content more than 0.8 (x > 0.8). In another study, Zhang, Fu et al. (2009) have investigated the effect of Aluminum contents on vacuum arc melted CoCrFeNiTiAl_x alloy systems with molar ratio of Aluminum (x) as 0, 0.5, 1, 1.5, 2 respectively [16]. The XRD analysis of the samples showed combinations of fcc and bcc structures. The phase composition transformed from a single fcc structure to stabilized bcc structure as the aluminum contents increased.

Lin and Tsai (2011) have investigated the microstructure, hardness, and corrosion properties of as-cast CoCrFeNiAl_{0.5} high-entropy alloy at normal temperature and aged at 350⁰C, 500⁰C, 650⁰C, 800⁰C and 900⁰C respectively [45]. They found significant effect of temperature on the XRD graphs of the HEA system. Result showed that as-cast CoCrFeNiAl_{0.5} alloy possesses an FCC solid solution matrix and droplet-shaped Al-Ni rich phase. However, at aging temperatures, alloys contain an fcc + bcc solid solution matrix with wall-shaped phases, droplet-

shaped phases and needle-shaped phases. The aging process caused the amount of Al-Ni rich droplet-shaped phases to be reduced.

2.2 Microstructural Morphology of HEA

Scanning Electron Microscopy (SEM) pictures are used to analyze the grain and cell structures of alloy more precisely. Cantor, Chang et al. (2004) have found from their study of multicomponent alloy systems that five-component equimolar FeCrMnNiCo alloy solidifies dendritically having an fcc structure [3]. When they added more metal elements and made different six to nine element component alloys, they found still they exhibit fcc based dendritic structure which can dissolve substantial amount of other transition metals. Their more careful study revealed that more electronegative metals such as Ge and Cu are rejected in inter-dendritic regions and less stable at dendritic area. Zhang, Fu et al. (2009) also found a dendritic morphology in their study on CoCrFeNiTiAl_x alloy system with varying aluminum contents [16]. In absence of aluminum content, the alloy system has a single phase. Aluminum addition caused the HEA system to have dendritic structure.

In an investigation on effect of iron content on wear behavior of AlCoCrFe_xMo_{0.05}Ni HEA by Hsu, Sheu et al. (2010), it was found that as the iron content was increased, the microstructure of the HEA system changed from dendritic (for $x = 0.6$ and 1) to poly grain (for $x = 1.5$ and 2) [46]. The dendritic, inter-dendritic and grains had two phases. While the dendritic region had less white phase, inter-dendritic phase mostly consisted of white phase.

In another study on AlCrFeCoNi HEA, Wang, Li et al. (2008) found from SEM analysis that the alloy has a polygonal grain microstructure with an intragranular dendritic segregation [22]. The fine microstructure of dendritic region is found to be nanoscale spherical precipitates

morphology and the inter-dendritic segregation area is found to be basket-wave morphology. While dendritic area is found to be Al, Ni rich and Cr, Fe depletes, inter-dendritic area is rich of Cr, Fe and contains less Al, Ni. Zhu, Zhang et al. (2010) in their study on microstructure and compressive properties of AlCoCrFeNiMo_x multicomponent alloy found M_0 and $M_{0.1}$ alloy show single phase morphology [47]. When the content of molybdenum is increased, the alloy system shows typical laminar eutectic structure.

2.3 Mechanical Properties

Research works in the HEA field are mostly focused to discover superior mechanical properties in the multi-component alloys. Due to wide compositional variety of HEA system, their mechanical properties also vary significantly. Some of the important mechanical properties of HEA are discussed here.

2.3.1 Wear Behavior

Due to being comparatively cheaper than most of the superalloys, titanium alloys and impressive mechanical properties, HEA has shown potentials for being used in tools, molds and structural components which require good wear resistance. Wear properties of HEAs are mainly tested in adhesive and abrasive conditions. Chuang, Tsai et al. (2011) have investigated the adhesive wear behavior of $\text{Al}_x\text{Co}_{1.5}\text{CrFeNi}_{1.5}\text{Ti}_y$ with varying aluminum and nickel contents [48]. They found that $\text{Al}_{0.2}\text{Co}_{1.5}\text{CrFeNi}_{1.5}$ and $\text{Co}_{1.5}\text{CrFeNi}_{1.5}$ alloys show at least two times better adhesive wear resistance comparing to conventional wear-resistant steels SUJ2 and SKH51. They concluded that the reason for the excellent wear-resistant behavior of multicomponent alloys is due to excellent oxidation property and resistance to thermal softening.

Wu, Lin et al. (2006) have showed in their study on adhesive behavior of $\text{Al}_x\text{CoCrCuFeNi}$ high-entropy alloys that different aluminum content can affect the wear resistance of the alloy system [49]. While low aluminum content causes worn surface to be deeply grooved and produces big debris, high aluminum content causes high-entropy alloy to possess smooth worn surface and yields fine debris. In another study by Hsu, Sheu et al. 2010, the effect of iron content on wear behavior of AlCoCrFeMoNi high-entropy alloys is investigated [46]. It is found that with increasing amount of iron, the wear behavior decreases. In a study by Chen, Lin et al. (2006) on the effect of vanadium addition on the abrasive wear-resistance of $\text{Al}_{0.5}\text{CoCrCuFeNiV}_x$ HEA system, it is found that wear-resistance of the HEA system increased by 20 percent as the content of vanadium increases from $x= 0.6$ to $x= 1.2$ and remains stable beyond $x= 1.2$ [50].

2.3.2 Fatigue Behavior

One of the greatest potentials of HEA is in aerospace industry where different engine components of aircraft encounter continuous cyclic loading. That is why good fatigue behavior of HEA is needed. In a study by Hemphill, Yuan et al. (2012) on fatigue behavior of $\text{Al}_{0.5}\text{CoCrCuFeNi}$ HEA, they compared the fatigue behavior of the HEA sample with conventional alloys such as steels, titanium alloys, and bulk metallic glasses [51]. They found that while the lower bound fatigue ratio of HEA is comparable to those of steels, titanium and nickel alloys, it is superior to zirconium alloys and zirconium-based bulk metallic glasses. The upper bound of fatigue ratio shows that HEAs have significantly higher fatigue ratio than conventional alloys and glasses. Therefore, HEAs have a great potential in structural applications comparing to conventional alloys as it will perform better under cyclic loading.

2.3.3 Corrosion Properties

In extremely condition application, materials must have good corrosion resistance to provide continuous good performance. The corrosion resistance of HEAs is studied in both NaCl ad H₂SO₄ solutions. Some HEAs showed better corrosion resistance as 304 stainless steel in both solutions [52]. Hsu, Chiang et al. (2005) have investigated the corrosion behavior of FeCoNiCrCu_x in 3.5% sodium chloride solution [53]. They found that the increasing amount of copper in the HEA increases the localized corrosion tendency. The HEA showed a dendritic microstructural morphology where dendritic region is Cu-depleted and inter-dendritic region is Cu-rich. Thereby an active cell is created in the alloy with significant potential difference, and the galvanic action causes the corrosion in the alloy. In another study (Lee, Chen et al. 2007), the effect of content of boron on corrosion resistance of Al_{0.5}CoCrCuFeNiB_x HEA is studied [54]. This experiment was carried in H₂SO₄ solution. The result showed that the amount of corrosion in the HEA decreases as the content of boron increases in the alloy system.

2.3.4 High Temperature Properties

Many HEAs have shown very good high temperature properties such as hardness, yield strength etc. Some research works demonstrated changes of hardness of HEAs and conventional alloys when temperature is increased gradually [45, 55]. AlCoCr₂FeMo_{0.5}Ni and Al_{0.2}Co_{1.5}CrFeNi_{1.5}Ti HEAs have higher hardness at room temperature comparing to the conventional alloys (SKH51, SUJ2, Inconel 718). When temperature is increased, the hardness of all the alloys in the figure decrease. The decline of hardness of conventional alloy is steeper than that of HEAs.

Senkov, Wilks et al. (2011) in their study with $\text{Nb}_{25}\text{Mo}_{25}\text{Ta}_{25}\text{W}_{25}$ and $\text{V}_{20}\text{Nb}_{20}\text{Mo}_{20}\text{Ta}_{20}\text{W}_{20}$ alloys have found excellent high temperature property of the multi-component alloys comparing to two popular high-performance Ni-based superalloys- Inconel 718 and Haynes 230 [56]. All four alloys are heat treated at different temperatures. The result shows that while Inconel 718 shows very high yield strength at low temperature, its yield strength decreases very quickly with increasing temperature comparing to the HEAs. Above 800°C , both HEAs possess higher yield strength than Inconel 718 and they become stable till 1600°C .

2.4 Selective Laser Melting & Processing Parameters

Traditionally, HEAs are produced and processed by casting, powder metallurgy, arc melting, plasma arc sintering, forging, hot rolling [16, 22-25, 57-59]. However, these methods cannot produce complex shapes and ultrafine microstructures. As getting expected phase, crystal structure and microstructure is largely depended on fabrication processes, it is worth investigating different HEA fabrication processes. Recently, additive manufacturing is getting popularity in HEA research. AM technology can produce complex three dimensional near-net shaped components without dies which is not possible by the conventional methods[60]. Selective laser melting, a novel AM technology, has been used in HEA and other alloy fabrication.

In SLM process, processing parameters such as laser type, laser power, spot size, scanning speed, hatch distance, layer thickness and scanning strategy significantly influence the quality of the final printed product. Several scientific studies [19, 61-65] found strong co-relation between microstructure and mechanical properties of SLM printed part and processing parameters of the SLM process. During the SLM process, the molten pool moves with the laser,

and temperature gradient in forepart of laser become much greater than the rear area due to lower heat conductivity of printed part comparing to untreated powder [66]. The temperature distribution in different areas of the powder bed changes very rapidly with the fast movement of laser beam, and it keep changing depending on time and space [67]. During the SLM process, scanned layers go through rapid thermal cycles. Residual stresses grow due to the resultant temperature gradient and the printed part deforms nonuniformly [68]. Proper selection of processing parameters is therefore required to get the quality product with expected microstructure, properties and densification [69, 70].

2.4.1 Laser Scanning Strategy

Laser scanning strategy is the specific patterns which define the spatial movement of the laser during the SLM process. Distribution of temperature on a melt pool depends on the laser scanning strategy. Laser scanning paths determine the temperature gradient and resulting stresses on a sample. Selecting appropriate scanning strategy is crucial to manufacturing high quality product without any defects. Inappropriate scanning strategies may cause nonuniform distribution of temperature and uneven stresses which are responsible for distortion or warpage of final part.

The number of research work done on scanning strategy has increased very rapidly over last decade [71]. Extensive research has been done to improve the print quality by adjusting the scanning strategy. Lu et al. [69] investigated the effect of scanning strategy with different island sizes on the microstructure and properties of SLM printed Inconel-718 alloy. While the density of printed samples increased island sizes, larger island samples experienced more residual stresses. By considering relative density, residual stress, and mechanical properties of the

samples, they found sample with 5×5 mm² scanning strategy optimal for their intended application.

Ramos et al. [72] worked with unidirectional, zigzag and alternating scanning paths. Due to the scan sequence in alternating scanning strategy, heat was more evenly spread throughout the layer and resulted a symmetric deformation while other two strategies produced asymmetric deformation. In contrast to unidirectional and zigzag strategies, alternating strategy could reduce the deformation of the printed part by 18.4% and 9.3% respectively. In case of alternating strategy, defining the sequence of scan vectors was found very significant for part deformation. Besides, based on their experiment with island scanning strategy, they found shorter vector scans resulted lower residual stress and lower deformation.

According to Zou et al. [73] while sweeping scanning direction had very little effect on residual stresses, adjusting scanning sequence could significantly reduce residual stress on a part comparing to unidirectional and alternating scanning strategies. They defined a “two-zone technique” scan strategy where, in the first sweep, laser scanned tracks had a large hatch spacing which resulted very low residual stress as there were minimal constraints between adjacent tracks. In the second sweep, laser scanned between two previously scanned solidified tracks. Higher heat conductive solid tracks reduced heat deposition in new tracks and new tracks experienced narrower melt pool and less shrinkage during solidification, which ultimately reduced total residual stress in the final part.

2.4.2 Scanning Direction

Scan direction has a significant role in creating good quality product by SLM. Wang et al. [74] produced SLM AlSi10Mg parts using two scanning strategies: a) horizontal sequential

pattern - laser moves in X-direction, b) declining sequential pattern - laser moves at a certain angle with X-direction. They measured residual stresses developed in X and Y directions for both patterns and found horizontal sequential pattern generated part with much improved residual stresses in both directions comparing to other strategy.

Rotation of scan direction is one of the important scan strategies which significantly influences morphological and crystallographic textures of a 3D printed part. As indicated by AlMangour et al. [75], scanning of subsequent layers without rotation of scanning direction created materials with anisotropic properties. They rotated the scanning direction by 90° inside a layer or between layers and found rotation of scanning direction resulted isotropic materials. In an investigation by Thijs et al. [76], they found a strong fibrous texture grew during SLM process of AlSi10Mg without changing scanning direction. However, the texture of the part changed when the scanning direction was rotated by 90° and a weak cubic texture along the building and scanning direction was found.

To understand the effect of rotation of scanning direction on the mechanical properties of Inconel 718, Trosch et al. [77] built their samples using three scanning orientations such as horizontal, vertical and 45°. They found horizontal built specimen showed the highest average tensile strength and the specimen with 45° rotation had shown the lowest average tensile strength. Scanning rotation strategy also found have effect on cracking in an investigation by Guo et.al [32]. They manufactured FeCoCrNiMn HEA using two 45° and 67° scanning rotations. They found 45° scanning rotation strategy created microstructures with dominant epitaxial growth of columnar dendrites and withstanding local strain and low strength which resulted higher crack densities comparing to 67° scanning rotation strategy.

2.4.3 Hatch Spacing

Hatch spacing has a strong influence on 3D printed part quality. An appropriate hatch spacing is very important for fabricating 3D samples with high relative densities and good surface finish [78]. The remelting area of the adjacent tracks are determined by the hatch spacing which influences the grain size and morphology[79, 80]. With increasing hatch spacing, the overlap between adjacent scan tracks decreases and more porosity develops which results lower density and rough surface during SLM process.

In a study by Pupo et al. [81] it was found that lower scan spacing created smooth and continuous surfaces regardless of the power and scanning speed. In their experiment, they used different scan spaces and found lower scan space value gave best performance in terms of surface smoothness due to heat accumulation effect. Lower scan spacing induced accumulation of heat from the previous track to the adjacent scanned track. This mechanism elongated the cooling time of scanned track and facilitate formation of continuous layer with sufficient overlapping. However, higher scan spaces created discontinuous isolated tracks. Similar result was found in another investigation by Aboulkhair et al. [82]. In their experiment, they used 5 hatch spacing values (50, 100, 150, 200 and 250 μm) and lower hatch spacing created good surface with good overlapping.

2.4.4 Scan Vector Length

Scanning vector length plays an important role in SLM process. During the scanning with long scan vector, larger portion of heat accumulated in melt pool can easily diffuse to environment by convection before the melting of the adjacent track. Therefore, larger scan vector leads to higher cooling rate of melt pool and lower average surface temperature. On the contrary,

shorter scan length facilitates higher temperature in the adjacent area of melt pool and promotes more uniform temperature distribution throughout the built surface. When short scan vector is used, there is a very short time difference between two successive track melting and heat from a melt pool doesn't get enough time to diffuse away. Rather, most of the heat is distributed among the melted tracks and helps to elevate the overall surface temperature. Higher surface temperature minimizes temperature gradient, reduces thermal expansion mismatch, and decreases cooling rate in the melt pool area and consequently residual stresses decrease. However, adjusting the scan length doesn't influence the total build time as the energy beam still travels the same length during scanning a single layer.

Unidirectional and bi-directional/zigzag scanning strategies are the most common scanning strategies where the only difference between them is the scanning direction. While the energy beam moves from the same direction in unidirectional strategy, in bi-direction strategy two adjacent scan vectors are opposite to each other. Though the bi-directional strategy has some advantages over unidirectional strategy, both strategies have limitations due to their long scanning length as discussed above. There is another scan strategy known as chessboard/island scanning strategy in which a single layer is divided into small square cells called islands. These small islands require shorter scan vectors and alleviate residual stresses.

Excessive residual stress creates part distortion, failure, and cracking of recoating blade. 3D product fabricated by selective laser melting is expected to have minimal residual stress. Studies have found that using shorter scan length can help minimizing residual stresses [83]. Therefore, in this study we are going to investigate the melting of CuCrFeNiTiAl alloy using different scan vectors under different energy input and effect of the different parameters on the microstructure and mechanical properties of this alloy.

CHAPTER III

METHODOLOGY

3.1 Materials

The CuCrFeNiTiAl_{2.5} and CuCrFeNiTi HEA were produced using 99.9% pure Cu, Cr, Fe, Ni, Ti and Al elemental powders. SEM pictures of all the powders are shown in Figure 1. The raw materials ordered from Sigma-Aldrich corporation were granular type. All the powders except Ti were found agglomerated. Only titanium powders were observed as round particle shape. All the physical details of all the elemental powders are provided in Table 1.

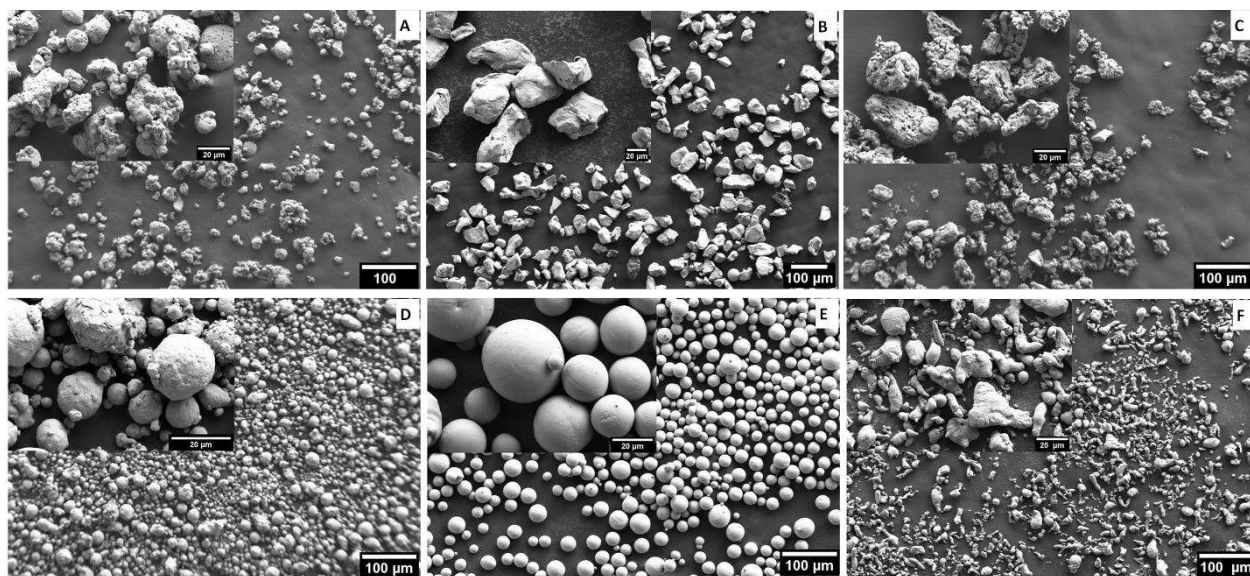


Figure 1: SEM pictures of raw metal powders (A) Cu, (B) Cr, (C) Fe, (D) Ni, (E) Ti, and (F) Al

Table 1: Physical properties and details of elemental metal powders

Property						
Chemical Formula	Al	Cr	Fe	Ti	Cu	Ni
Molar mass [g/mol]	26.98	52	55.85	47.87	63.55	58.69
Density [g/cm ³]	2.7	7.19	7.87	4.51	8.96	8.91
Molar Heat Capacity [J/(mol K)]	24.2	23.35	25.1	25.06	24.44	26.07
Melting Temperature [°C]	660.32	1907	1538	1668	1084.62	1455
Boiling Temperature [°C]	2470	2671	2862	3287	2562	2730
Supplier Company	BTC	BTC	BTC	Sigma Aldrich	BTC	BTC
Purity	99.50%	99.00%	98.00%	99.00%	99.00%	99.50%
Particle Size [µm]	< 45	< 45	< 45	< 45	< 45	< 37

3.2 Powder Mixing

Elemental powders were mixed in an oxygen-free chamber with Argon atmosphere. The nominal composition of different metals in the CuCrFeNiTiAl_{2.5} and CuCrFeNiTi HEA samples are given in Table 2 and Table 3 respectively. For getting homogeneous mixture, the mixed powder was placed on a V-type blender and rotated for 2 hours at 200 rpm.

Table 2: Powder mixing protocol of CuCrFeNiTiAl alloy system

	Cu	Cr	Fe	Ni	Ti	Al
Weight %	22.29	18.24	19.59	20.59	16.79	2.5
Molar Ratio	0.19	0.19	0.19	0.19	0.19	0.05

Table 3: Powder mixing protocol of CuCrFeNiTi alloy system

	Cu	Cr	Fe	Ni	Ti
Weight %	22.86	18.71	20.09	21.12	17.22
Molar Ratio	0.2	0.2	0.2	0.2	0.2

3.3 AM Fabrication

3.3.1 5X5 Test Series of CuCrFeNiTiAl HEA

To investigate the effect of different printing parameters on the microstructure and crystal growth of the CuCrFeTiNiAl_{2.5} alloy, a 5 × 5 test series (Figure 2) was designed with different laser power (100-200 W), exposure time (20-80 μS) and point distance (40-60μm) as mentioned in Table 4. Each block (5mm x 5mm) of the test series was printed up to 12 layers using a Renishaw AM250 on a single 316L stainless steel substrate. A unidirectional meander build strategy was selected with a hatch distance of 0.09mm. The amount of energy generated from laser depends on the printing parameters. Energy density of laser in different blocks as illustrated in Table 5 was calculated by the following formula [84]:

$$\text{Energy Density, } E_A = \frac{\text{Laser Power (W)}}{\text{Scanning Velocity (mm/s)} * \text{Scan/Hatch Distance (mm)}} \text{ J/mm}^2$$
$$= \frac{\text{Laser Power (W)} * \text{Exposure Time (μS)}}{1000 * \text{Point Distance (μm)} * \text{Scan/Hatch Distance (mm)}} \text{ J/mm}^2$$

The SLM process starts with preparation of the process chamber by selecting proper oxygen level, inert gas pressure and thermostat temperature from a human-machine interface (HMI) touchscreen. In this experiment, oxygen concentration inside the chamber was set 500 ppm (parts per million) and high purity argon gas with a line pressure of 1bar was used as inert media. For facilitating proper melting of the first powder layer, the build substrate was preheated to 170⁰ C. When the process chamber was ready, the mixed powder was applied using a manual powder deposition procedure from a low-profile hopper developed at author's lab. The re-coater blade distributed the powder on top of the build substrate in a uniform thin layer. The high energy laser emission was then redirected to the build plate using an optical scanner to melt the

powder and produce the contour of all 25 blocks. After printing each layer of the blocks, the build plate went down a layer thickness and more powder was feed to the build plate to start printing another layer. Thereby all sample blocks were built layer by layer. As soon as the build was complete, the build chamber cooling process got started. Once the heater temperature reached to room temperature, the printed part was taken out and cleaned of any excess powder.

Table 4: 5X5 test series design

Point Distance (μm) →		60	55	50	45	40
Power(W)↓	Exposer (μS)↓					
100	20	1A	1B	1C	1D	1E
125	35	2A	2B	2C	2D	2E
150	50	3A	3B	3C	3D	3E
175	65	4A	4B	4C	4D	4E
200	80	5A	5B	5C	5D	5E

Table 5: Energy density (J/mm²) of 5X5 Test Series

Point Distance (μm) →		60	55	50	45	40
P (W)↓	Exposer (μS)↓					
100	20	0.37	0.40	0.44	0.49	0.56
125	35	0.81	0.88	0.97	1.08	1.22
150	50	1.39	1.52	1.67	1.85	2.08
175	65	2.11	2.30	2.53	2.81	3.16
200	80	2.96	3.23	3.56	3.95	4.44

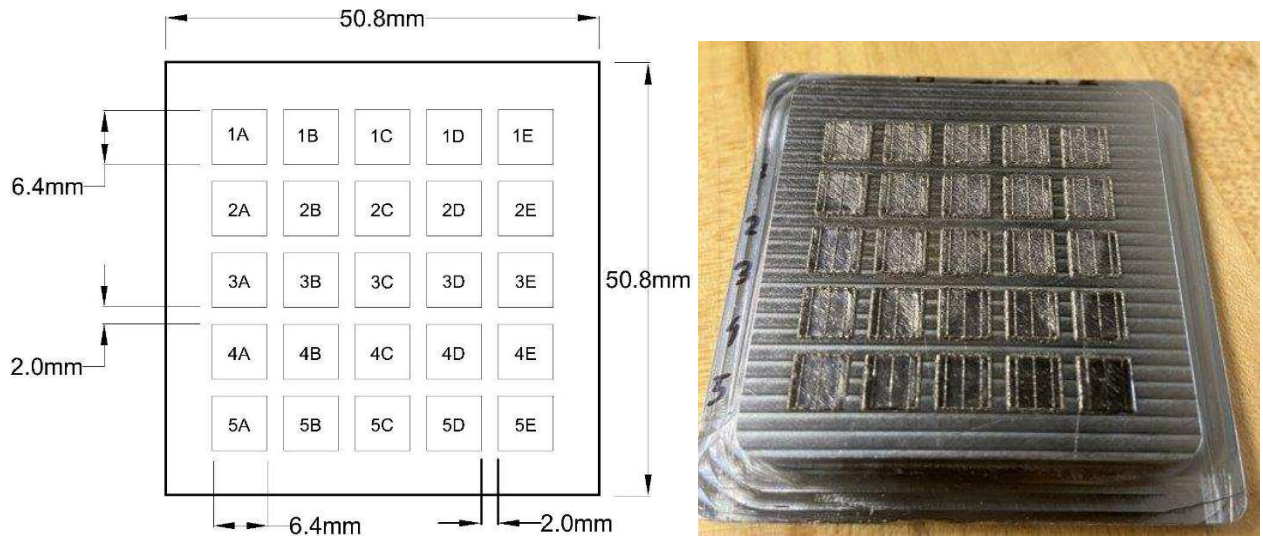


Figure 2: (a) Detailed dimension 5X5 of the test series (b) SLM printed part

3.3.2 3X3 Test Series of CuCrFeNiTiAl & CuCrFeNiTi HEA

To investigate scan length strategy a 3X3 test series is designed. A Taguchi design is done in Minitab where 4 factors such as laser power, hatch distance, point distance, and exposure time are considered each factor having 3 different levels. Practically a total 3^4 or 81 number of parameter combinations are possible when there are 4 factors each having 3 levels. But the Taguchi design efficiently reduced the number to only 9. In all the 9 runs a constant layer thickness of 60 μm is used. Details of the Taguchi design and the parameters setting with energy densities of the test series are given below.

Design Summary

Taguchi Array

$L9(3^4)$

Factors: 4

Runs: 9

Columns of $L9(3^4)$ array: 1 2 3 4

Table 6: Parameter settings for 3X3 test series according to Taguchi design

Run	Power (W)	Hatch Distance (μm)	Point Distance (μm)	Exposure Time (μs)	Layer Thickness (μm)	Energy Density (J mm^{-3})
1	150	90	40	50	60	34.72
2	150	105	45	65	60	34.39
3	150	120	50	80	60	33.33
4	175	90	45	80	60	57.61
5	175	105	50	50	60	27.78
6	175	120	40	65	60	39.5
7	200	90	50	65	60	48.15
8	200	105	40	80	60	63.49
9	200	120	45	50	60	30.86

In the 3X3 test series design, each individual parameter set or run scans HEA 4 samples with 4 different widths 0.5 mm, 0.75 mm, 1 mm, and 1.5 mm respectively. As a meander hatch strategy is used in this experiment, width of the samples worked as the scan lengths of the respective samples. The full test design is illustrated in Figure 3.

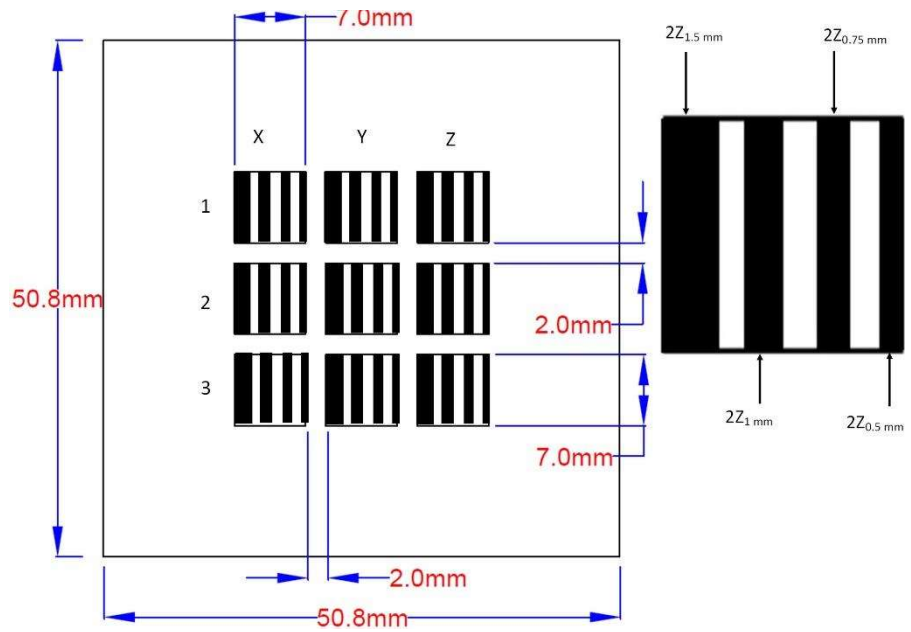


Figure 3: Detailed dimension of 3X3 test series



Figure 4: SLM printed 3X3 test series

3.4 Testing Method

The phase structures of CuCrFeTiNiAl_{2.5} alloy samples were evaluated by X-ray diffraction (XRD). A Bruker D8 X-ray diffractometer with a Cu K_α radiation (wavelength, $\lambda = 1.5406 \text{ \AA}^0$) was operated at 40 kV voltage with the current of 40 mA to identify phase structures. The radiation scanned sample surfaces continuously with a locked coupled step size of 0.01⁰, a speed of 1.17⁰ min⁻¹ and 2θ between 10⁰ and 80⁰. The XRD profiles found after scanning were analyzed by Crystallographica Search-Match (CSM) program developed by Oxford Cryosystems [85]. Finally, Origin Pro program was used to sketch a schematic illustration of the crystal structures. To characterize morphology and microstructures, images on the surface of the blocks were taken using Carl Zesis Sigma VP Scanning Electron Microscope (SEM). Average length point distance and area of bright phases found on SEM images on nanoscale were calculated using imageJ software. Energy Dispersive X-ray Spectroscopy (EDX) detector on the SEM model was used to identify the composition weight and atomic ratio of metal elements available in different blocks.

To investigate the surface quality and hardness of the CuCrFeTiNi HEA, larger specimens were fabricated by the SLM process as shown in Figure 5. The four specimens designed for testing purpose are 2Y_{0.5}, 2Y_{1.5}, 2Z_{0.5}, and 2Z_{1.5}. All the specimens were printed using the processing parameters set previously for them. While for 3X3 test series a meander hatch strategy was used, a stripes hatch strategy was utilized for printing the test specimens with each individual stripe having a field length of the respective sample scan lengths.

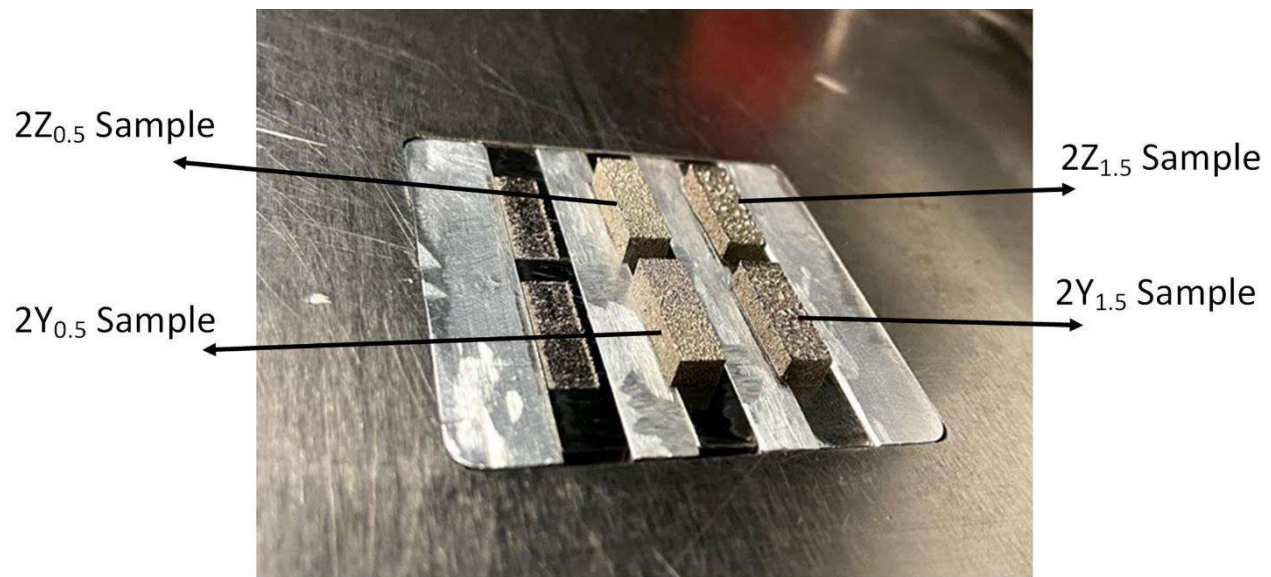


Figure 5: Specimens printed for surface roughness and micro-hardness measurement

CHAPTER IV

RESULT AND DISCUSSION

For the convenience of testing and analysis purposes of the research work, a selected number of samples were taken in consideration out of all the printed samples for further investigation. From the 5X5 test series, sample 1A, 3C, and 5E were selected to see the effect of different energy densities on the HEA microstructures. From the 3X3 test series, 2Y and 2Z samples were selected for investigating the effect of scan vector lengths on HEA build. Rest of the samples in the 3X3 test series were found have very poor build quality as shown in Figure 6.

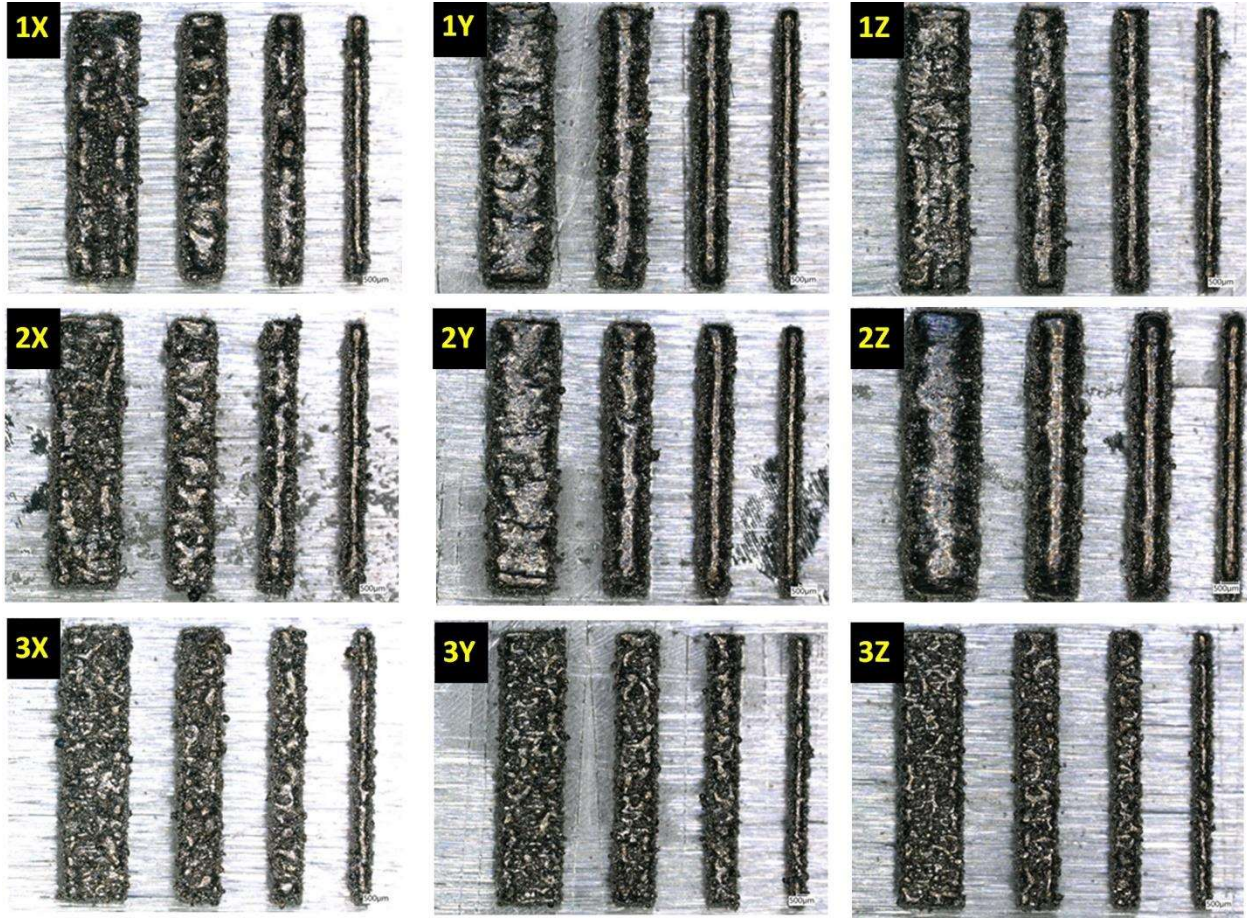


Figure 6: Pictures of 3X3 test series samples after laser melting process of CuCrFeNiTi HEA

4.1 XRD Analysis

The XRD measurements were carried out to examine the crystal structures of the SLM as-built CuCrFeNiTiAl HEA samples. Figure 7 shows the XRD patterns of different samples. All XRD plots have been corrected for background noise and five strong peaks are visible in the 2θ range from 10° to 80° . The result shows that all five samples consist of three different crystal phases: face-centered cubic (FCC), body-centered cubic (BCC), and hexagonal. The alloy system comprises a major FCC and BCC solid solution matrix. Two major peaks were found at 2θ between 42° and 45° with FCC and BCC crystal structures, respectively. High peak responsible for FCC structure in LEDA, MEDA, HEDA, 2Y, and 2Z samples, with intensities of

222 ($2\theta = 42.78^\circ$), 282 ($2\theta = 42.63^\circ$), 383 ($2\theta = 42.85^\circ$), 46.96 ($2\theta = 42.07^\circ$), and 38.96 ($2\theta = 42.01^\circ$) respectively. Similarly, for BCC structure indicating high peaks in five samples, respective intensities are 127 ($2\theta = 43.52^\circ$), 210 ($2\theta = 43.56^\circ$), 404 ($2\theta = 43.54^\circ$), 53.44 ($2\theta = 43.59^\circ$), and 52.16 ($2\theta = 43.6^\circ$).

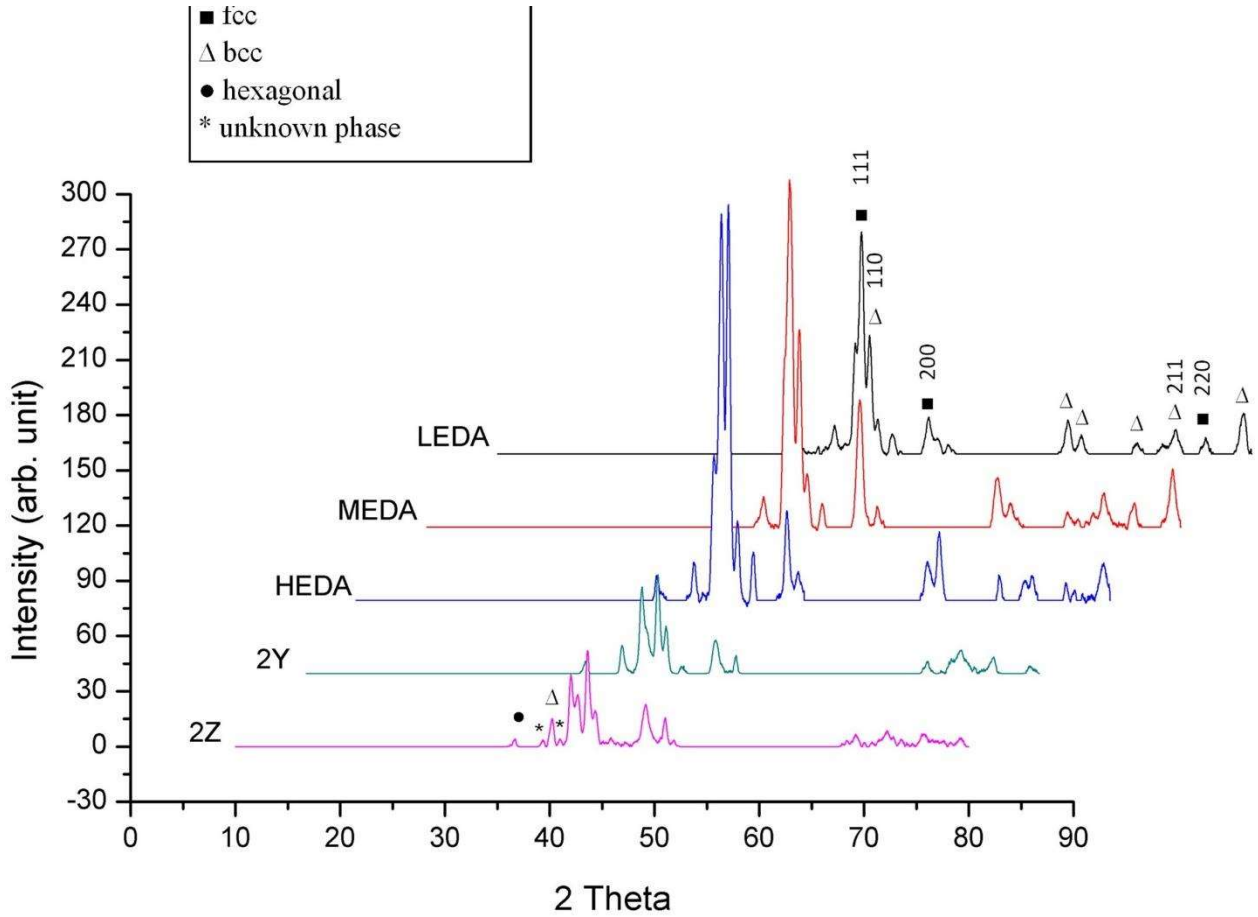


Figure 7: XRD patterns of CuCrFeNiTiAl HEA samples under different energy densities (LEDA, MEDA, & HEDA) and of CuCrFeNiTi HEA samples (2Y & 2Z).

LEDA, MEDA, and HEDA samples contain Al and with increasing energy input during the laser melting process, the intensity of major XRD peaks and other minor peaks have increased. However, two peaks identified for FCC phase at $2\theta = 47^\circ$ - 52° has higher intensity at mid-energy density area sample compared to high and low energy density area samples.

However, in case of samples without Al, highest intensities of peaks were found in the sample 2Y comparing to the highest energy density area sample 2Z. The most obvious distinction between the samples with Al and without Al was the BCC peaks at $2\theta = 60^\circ$ - 65° . Two such BCC peaks were found at this position in samples without Al, but those were absent in other samples.

4.2 Microstructure analysis

4.2.1 5X5 test series samples

Figure 8 (A) shows an example of low magnification SEM pictures of the CuCrFeNiTiAl samples. It can be noticed that the surface morphology shows non-uniform microstructural distribution, which is considered due to the blending procedure. Additionally, though most of the high entropy alloy systems developed using casting process exhibit dendritic structural morphology, the CuCrFeNiTiAl samples in this study exhibited fine grained structures.

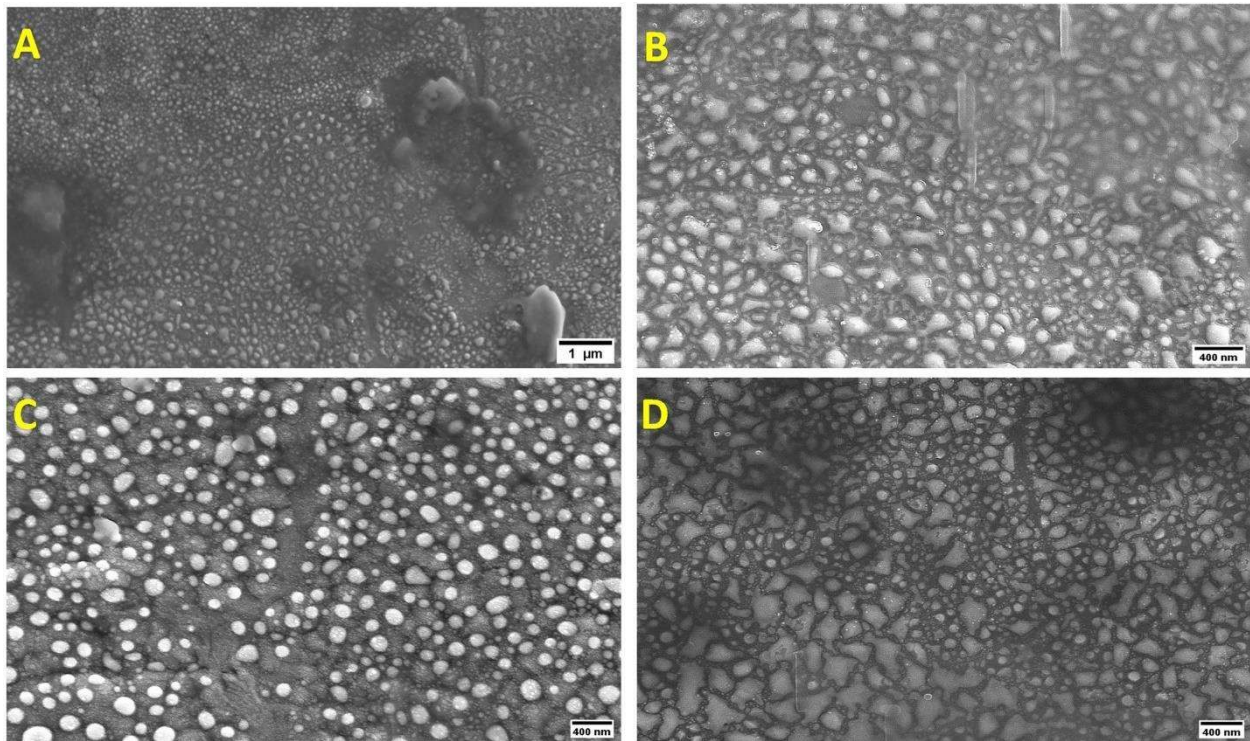


Figure 8: SEM pictures of CuCrFeNiTiAl sample of (a) 1A at low magnification; and samples of (b) 1A, (c) 3C, and (d) 5E at high magnification.

High magnification pictures of the samples were taken in specific regions of interest and multi-phase morphology was observed, as shown in Figure 8 (b-d). The two distinct structures identified as bright area and dark area, with noticeable difference in shape, size and distribution. The amount of the bright phases shows increasing with an increase of energy density. In addition, it was observed that the bright phases in Sample 1A and 5E have polygonal shape while round-shaped bright phase was observed in sample 3C.

Average length, point distance and area of bright phases are calculated using imageJ software. The mean length of the bright phase is the largest in the high energy density area (Sample 5E) which is 186.24 nm and the smallest mean length is developed in sample 3C (122.92 nm). The mean area of bright phases has increased with increasing laser energy input

during melting from 8989.82 nm^2 through 12857.71 nm^2 to 13016.14 nm^2 . The point distances are measured to depict the distribution of bright phases throughout the microstructure. It is found that comparing to other two samples, the bright phases are positioned more closely in sample 5E with a mean point distance of 93.72 nm .

4.2.2 2Y and 2Z samples with Al

In 2Y and 2Z samples, while hatch spacing was the same, they had different energy densities applied during laser melting. The microstructures of the samples with and without Al are discussed below.

4.2.3 Sample 2Z_{1.5} Vs Sample 2Z_{0.5}

First thing visible in samples are stripes appeared on the surface along the scanning direction. These stripes are not parallel to the scanned tracks. The reason behind the generation of these stripes is the overlapping between successive tracks. As soon as the laser melts the powder mixture, the molten material starts to flow around due to the gravitational effect. As the molten tracks and the overlapping areas have different heat accumulation, stripes not necessarily parallel to scan tracks appears.

Figure 9 shows the surface of all four different scan vector lengths sample 2Z. With the increasing scan vector length, the number of stripes also increased. During scanning with longer scan vector, the laser takes longer time to come back to remelt the just melted track. Usually, the remelting process helps to maintain liquid state of the previously melted track and facilitate better diffusion. As SLM has a very fast cooling rate, a very short time here can make a big difference. Shorter scan vector helps the previous track to maintain higher temperature, consequently better diffusion and therefore the number and length of stripes have reduced.

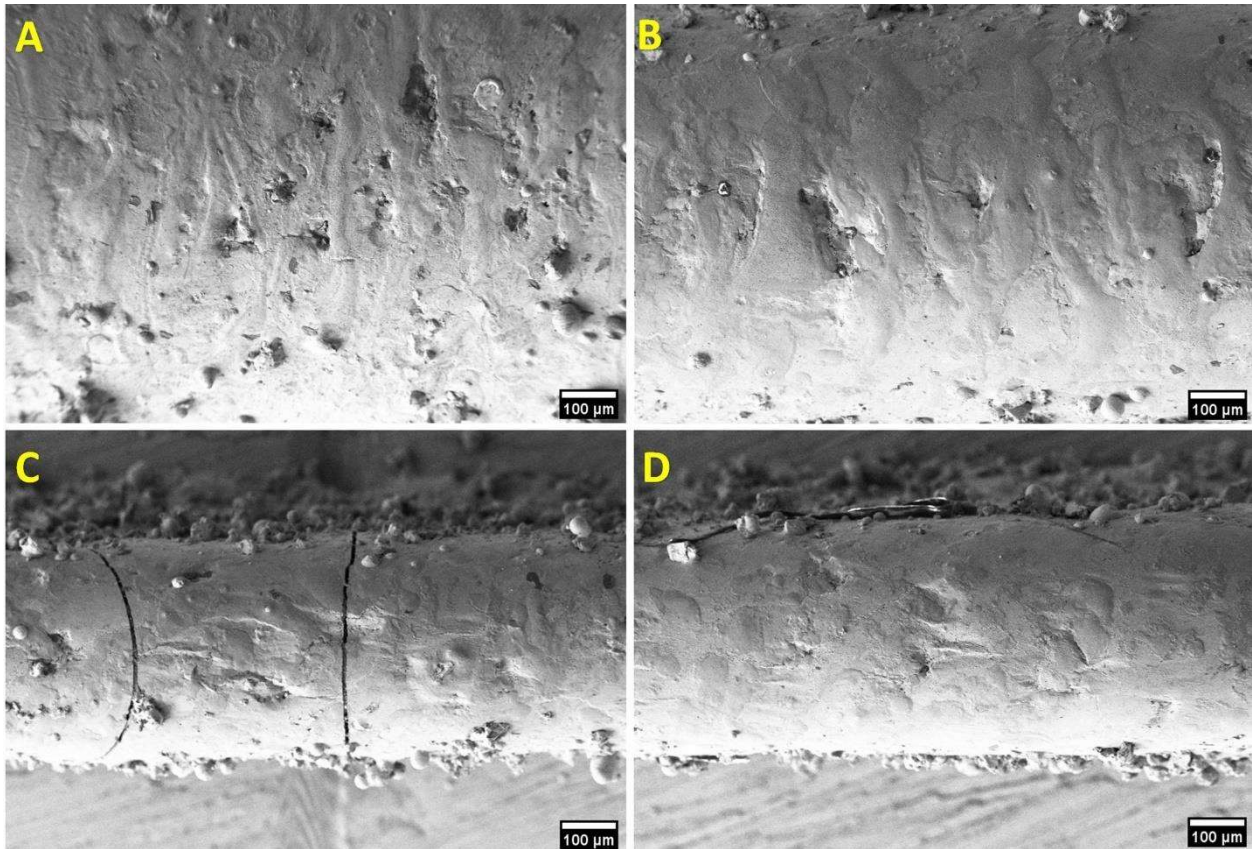


Figure 9: Surface of as built 2Z samples (with Al) with (A) 1.5 mm (B) 1 mm (C) 0.75 mm and (D) 0.5mm scan vectors

While comparing melt pools of different samples, shorter scan length showed better melting process. In 1.5 mm sample, there were greater number of powder particles not fully melted, but a smaller number of raw powders is observed in 0.5 mm sample. Besides, the lower scan length resulted more uniform microstructure. Higher scan vector generated non-uniform microstructure in the overlapping areas. There were four types of microstructures observed in the printed samples as shown in Figure 10 and Figure 11 such as dendrites, rosette, petals, and branches type structures.

In 1.5 mm sample, petal and dendritic morphologies were mostly observed. However, the dendritic grains were not fully developed in most of the surface area and their sizes were very

small. In 0.5 mm sample, presence of fully grown dendrites were seen with an average size of 4-8 μm . Besides, the presence of dendrites was prevailing in 0.5 mm sample. This was an evidence of comparative slower cooling rate in shorter scan sample which resulted from better temperature accumulation in melt pool. Research has found that with decreasing cooling rate, the grain size becomes larger during solidification process and the grain morphology changes from spherical to dendritic. Usually, HEA is manufactured by casting process where slow cooling allows dendritic structures to grow [86]. An interesting grain morphology was observed in both the samples which looks like branches of tree as shown in Figure 10 and Figure 11. These limited number of branches like structures were mostly developed in the overlapping areas of scanning tracks.

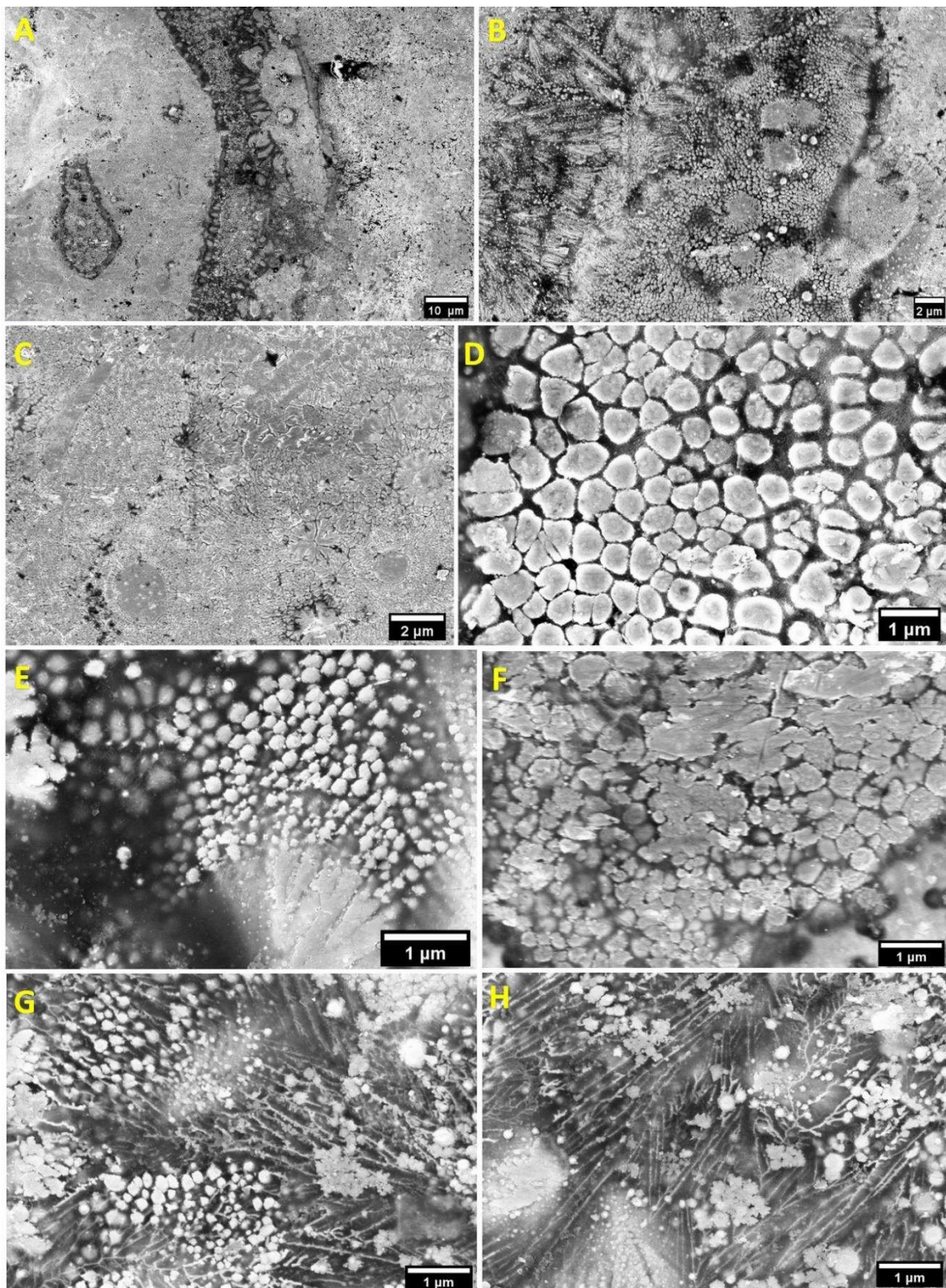


Figure 10: (A) Low magnification picture of $2Z_{1.5}$ sample, (B) rosette (C) dendritic, (D), (E), (F) petals, & (G), (H) branches structures

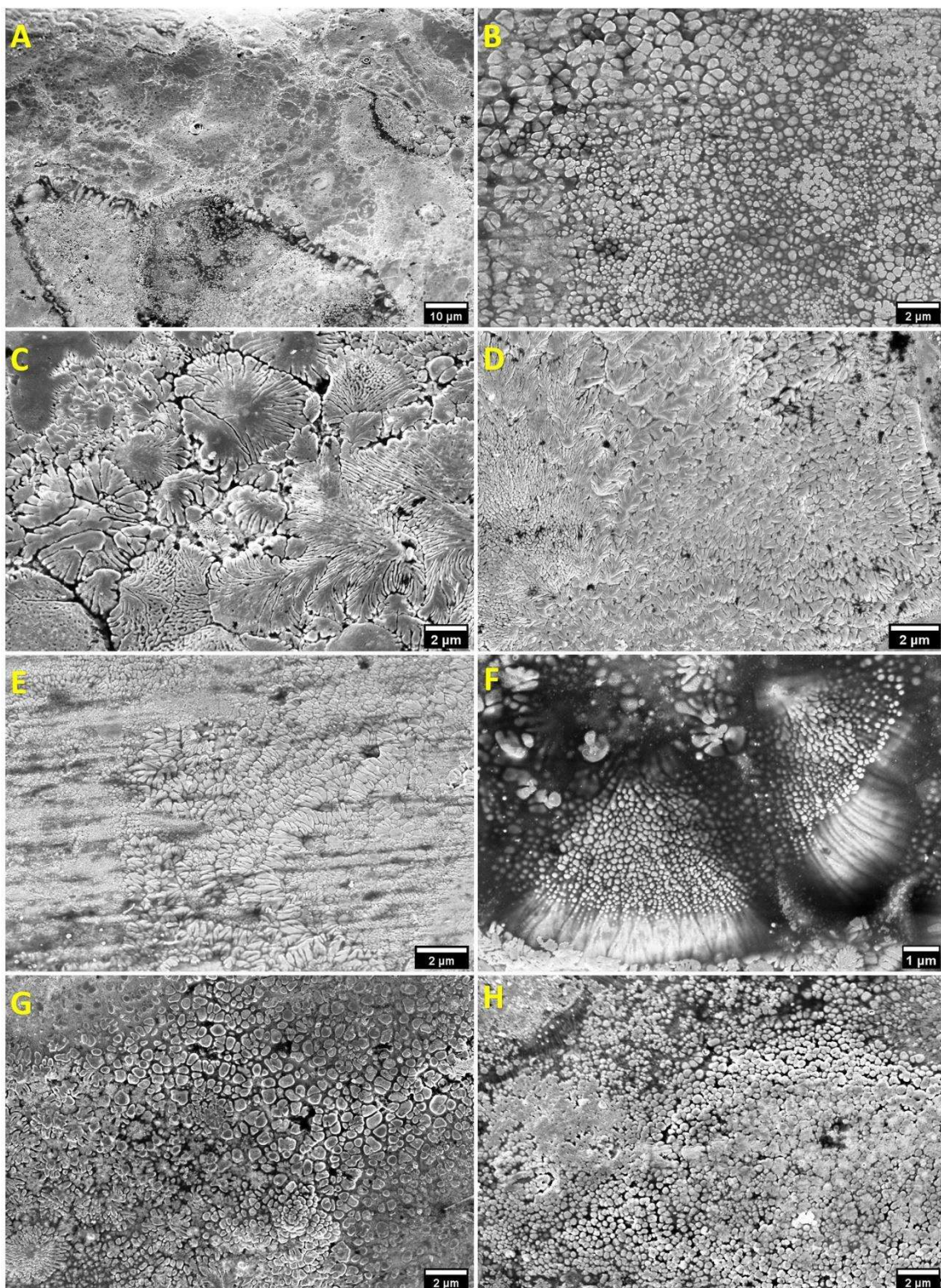


Figure 11: (A) Low magnification picture of $2Z_{0.5}$ sample, (B) petals (C), (D), (E) dendrites (F) & (G) petals with rosette (H) small petal structures

4.2.4 Sample 2Y Vs Sample 2Z

The boundary of the overlapping area in samples 2Z is wider and visible, and most of the overlapping area had dendritic morphology with some petal type grains as shown in Figure 12. Surface morphology in rest of the area were dendrites, rosette, petals. Average grain size of the dendrites was below 1 μm and petals were 0.63 μm on average. In contrast, mostly petal microstructures were enclosed in the overlapping area by a very thin boundary in sample 2Y (Figure 13). Rest of the area had dendritic microstructure with an average size of 3-6 μm . The growth of dendritic grains in 2Y sample implied the slower solidification of melt pool what allowed the grains to develop. However, there were comparatively higher number of porosities appeared in the overlapping area in the lower energy density 2Y sample due to the insufficient melting of the powder.

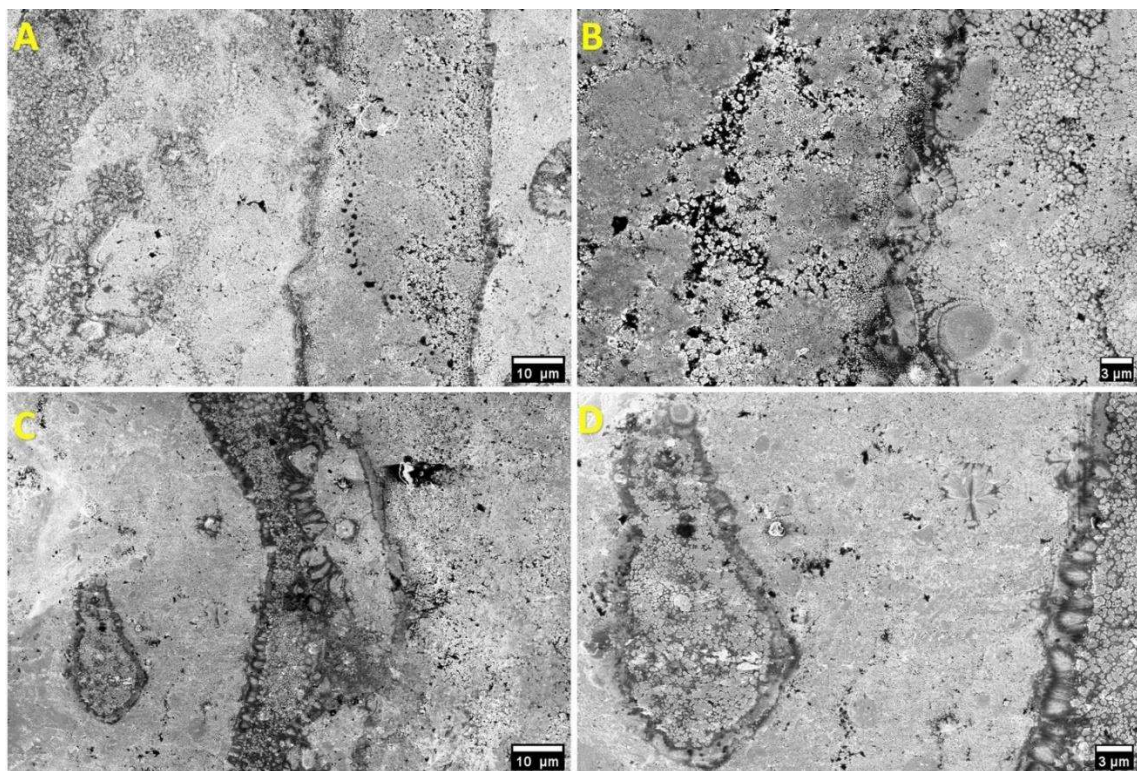


Figure 12: Microstructures in the stripe areas of samples (A) & (B) 2Y_{1.5}, (C) &(D) 2Z_{1.5}

The energy density in the 2Y sample was lower than that of 2Z sample. However, the laser scanned a 1.5 mm track in sample 2Y with exposure time and point distance of 50 μ s and 50 μ m respectively. Exposure time and point distance in sample 2Z were 80 μ s and 40 μ m respectively. At this parameter setting, the laser took approximately 1500 μ s and 3000 μ s to print a track in sample 2Y and sample 2Z respectively. Consequently, the subsequent tracks in sample 2Y could help previous tracks to accumulate temperature more effectively and the cooling time got elongated. Due to longer time difference between two subsequent tracks in sample 2Z, most of the heat of previous melt pool dissipated to surrounding and couldn't help in increasing the cooling time.

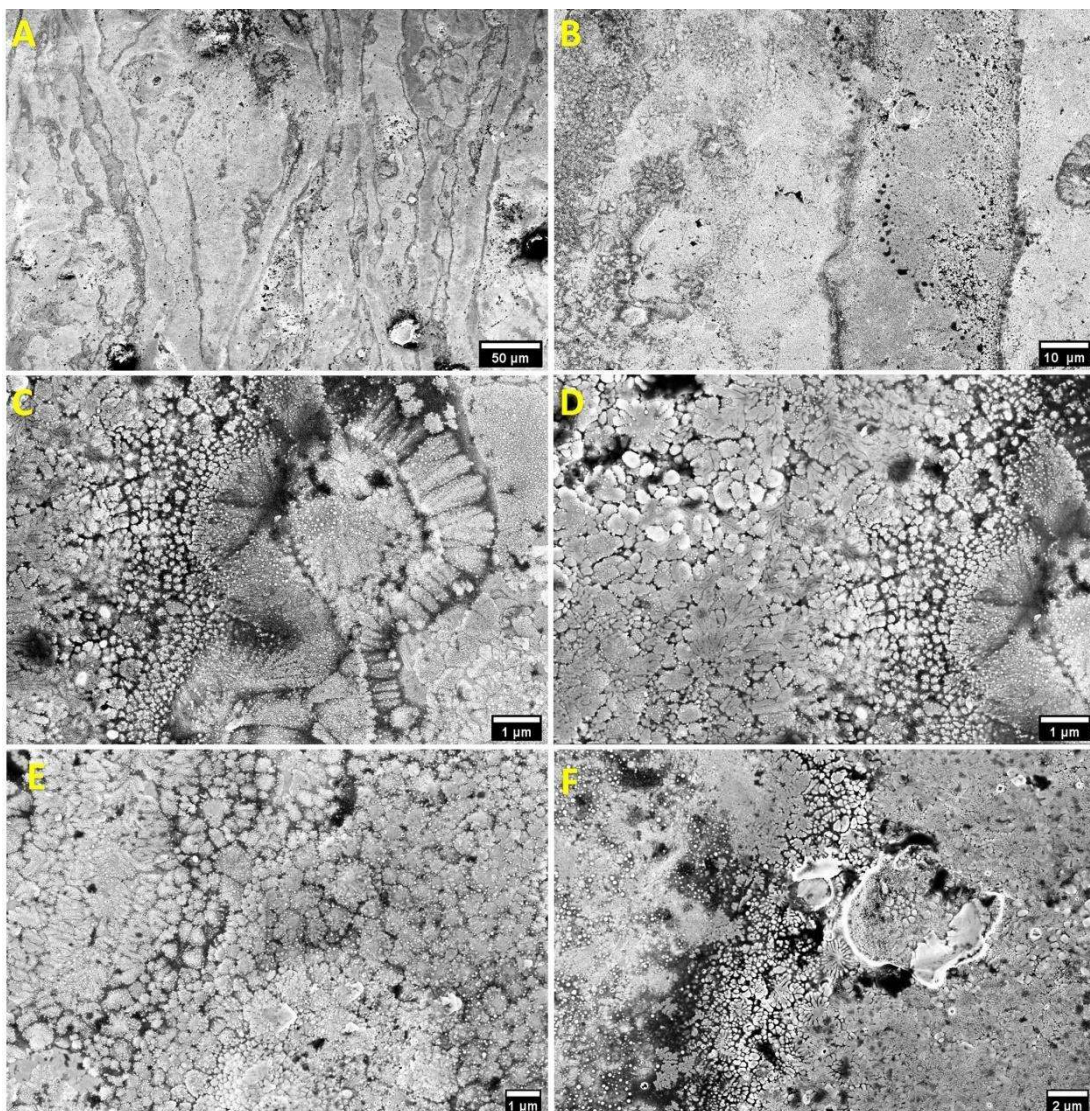


Figure 13: (A) & (B) Low magnification picture of 2Y_{1.5} sample, (C) & (D) petals, branches, and dendrites, (E) dendrites, (F) rosette structures with petals

4.2.5 2Z Samples Without Al

When comparing short and long scan vector 2Z samples without Al, the most visible difference was the grain morphologies. The shorter scan sample surface contained many dendritic grains while a very few dendrites were observed in 1.5 mm sample (Figure 14 and Figure 15). The larger scan sample mostly possessed very fine petal grains and some big petals.

The overlapping area in 1.5 mm sample didn't have any boundary. However, overlapping area was not identifiable in 0.5 mm sample which indicated better diffusion among the different elements. There was no stripe-like overlapping areas visible in both the samples without aluminum. Moreover, branches morphologies were absent in the samples without aluminum. Therefore, branches could be resulted due to presence of aluminum.

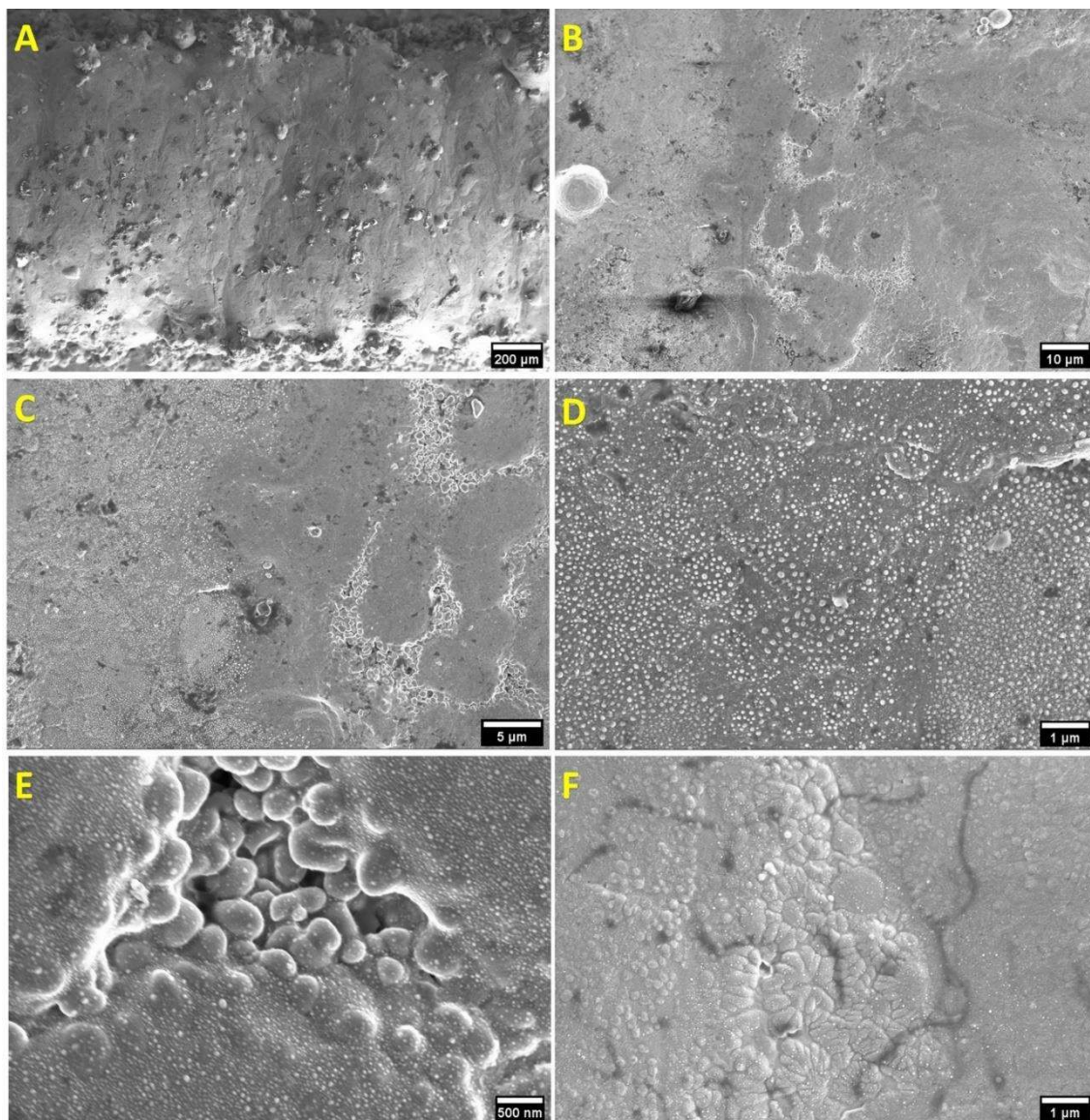


Figure 14: (A) low magnification picture of sample 2Z_{1.5} (B) & (C) melt pool and overlapping area interface, (D) small petals in melt pool area, (E) petals in overlapping, (F) dendritic structure

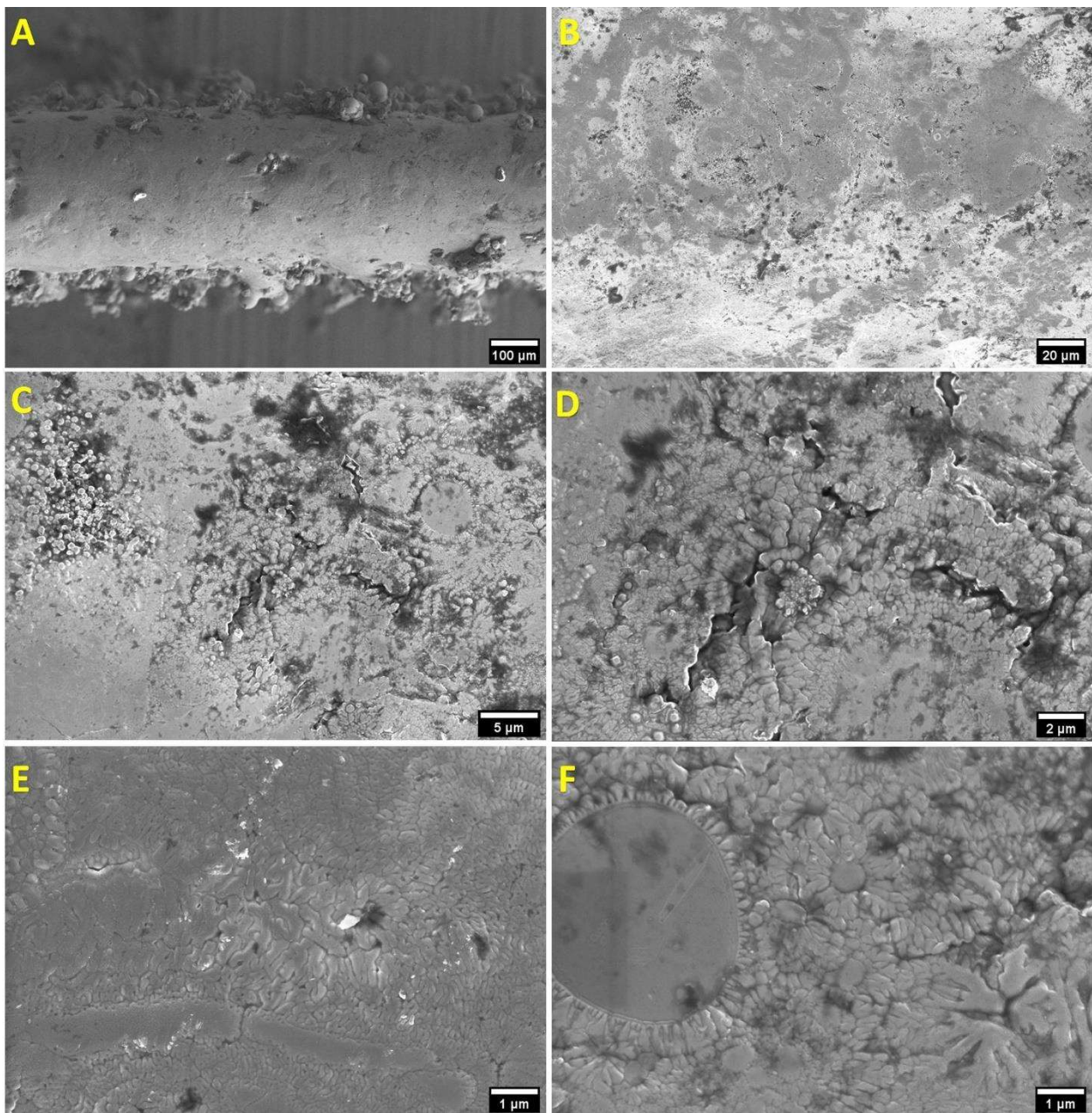


Figure 15: (A) & (B) low magnification pictures of sample 2Z_{0.5}, (C) petal and dendrites, (D) & (E) dendrites, (F) dendrites with rosette structures

4.3 EDX Element Analysis

4.3.1 Sample 1A, 2B, and 3C of CuCrFeNiTiAl HEA

EDX analysis was conducted for samples 1A, 3C, and 5E to find out elemental compositions in both bright and dark areas upon different energy densities. 7 shows the composition of metal elements from EDX analysis given at weight percentage. 16 shows the comparison of chemical composition in both bright and dark areas of the three samples with their nominal compositions. It is noticed that the EDX analyzed composition of each element was significantly different away from the nominal composition ratio, even though the elemental powder materials were pre-blended in equimolar ratio except for Al. Among all the principal elements, Cr has the lowest molar ratio, and the highest molar ratio is observed in case of Ti. The molar ratio of Cr, Fe and Ni are lower than the nominal molar ratio (19 %), and Ti is about twice amount of the nominal values. However, Cu is the only principal element whose presence in different sample areas is consistent with the nominal molar ratio. In all samples, the molar ratio of Al is slightly greater than 5 %.

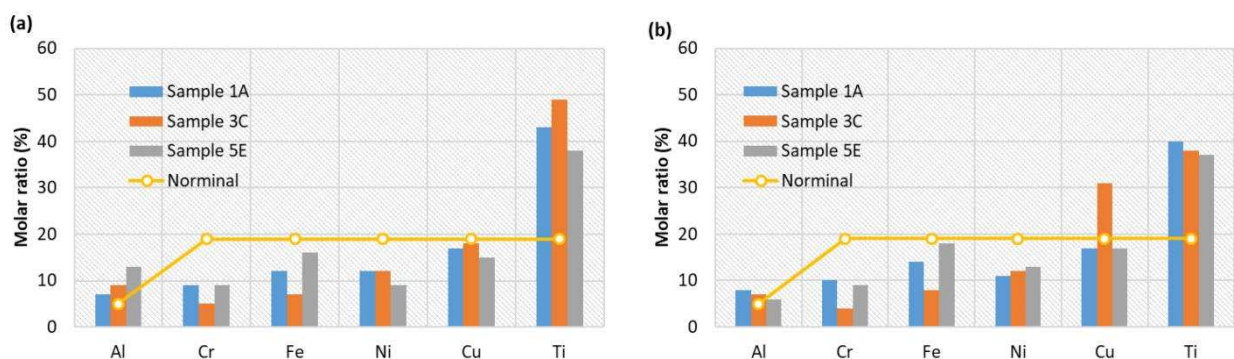


Figure 16. Chemical composition of (a) bright area and (b) dark area of CuCrFeNiTiAl samples.

When comparing between the bright and dark areas, a significant difference is noticed in Sample 3C that the bright area of Sample 3C shows rich of Ti element, while Cu is rich in dark area. This elemental segregation can be explained by mixing enthalpy of principal elements. As Cu has higher mixing enthalpy with other elements and mixing enthalpy of Ti is very low, Cu is repelled from the Ti-rich bright area [87].

Moreover, though principal elements were mixed in equimolar ratio, the EDX analysis of the CuCrFeNiTiAl sample fabricated in SLM process found no equimolar ratio in any sample in this study. It can be indicated that insufficient energy was deposited into the powder blend. The energy generated from laser during melting was from 5.29 KJ/mm³ to 63.49 KJ/mm³ and depending on the absorption rate of heat by the powder mixture, a portion of that energy is utilized for melting which might have not become sufficient enough heat to melt powder completely. Another reason was that the rapid cooling of the melt pool was not able to provide sufficient time window for the diffusion of the elements to form random solid solution.

Table 7: Chemical composition of CuCrFeTiNiAl2.5 alloys in bright and dark areas.

	Al	Cr	Fe	Ni	Cu	Ti	Total
Block 1A							
Nominal	0.05	0.19	0.19	0.19	0.19	0.19	1.00
Bright	0.07	0.09	0.12	0.12	0.17	0.43	1.00
Dark	0.08	0.10	0.14	0.11	0.17	0.40	1.00
Block 3C							
Nominal	0.05	0.19	0.19	0.19	0.19	0.19	1.00
Bright	0.09	0.05	0.07	0.12	0.18	0.49	1.00
Dark	0.07	0.04	0.08	0.12	0.31	0.38	1.00
Block 5E							
Nominal	0.05	0.19	0.19	0.19	0.19	0.19	1.00
Bright	0.13	0.09	0.16	0.09	0.15	0.38	1.00
Dark	0.06	0.09	0.18	0.13	0.17	0.37	1.00

4.3.2 Sample 2Y and 2Z of CuCrFeNiTiAl HEA

From EDS mapping of samples 2Y and 2Z (Figure 17 & 18), it is found that Ti and Cr were mostly uniformly distributed throughout the non-uniform morphologies. However, in sample 2Y, amount of Ti and Cr in dendrites were not as it was in other part. Fe, Ni, and Cu were more densely distributed in dendrites and mostly depleted from petals. Al is found mostly segregated in petals, depleted from dendrites. Similar result is found in the large-scale picture of sample 2Z except Ti and Cr were more uniformly both in petals and dendrites. However, in the magnified picture (Figure 19) of the same sample in dendritic area shown that Ti and Cr were not distributed uniformly as the sample 2Y, instead they are mostly segregated in dendrites and Fe, Ni, and Cu are segregated more in inter-dendrites. The reason behind this can be the asymmetry in the melting temperatures of the different elements which encourages Ti and Cr to solidify first

in the dendritic cores forcing Fe, Ni, and Cu into the inter-dendritic region. The depletion of Fe, Ni, and Cu from the petals dendrites can be verified also from the EDS result from table 8.

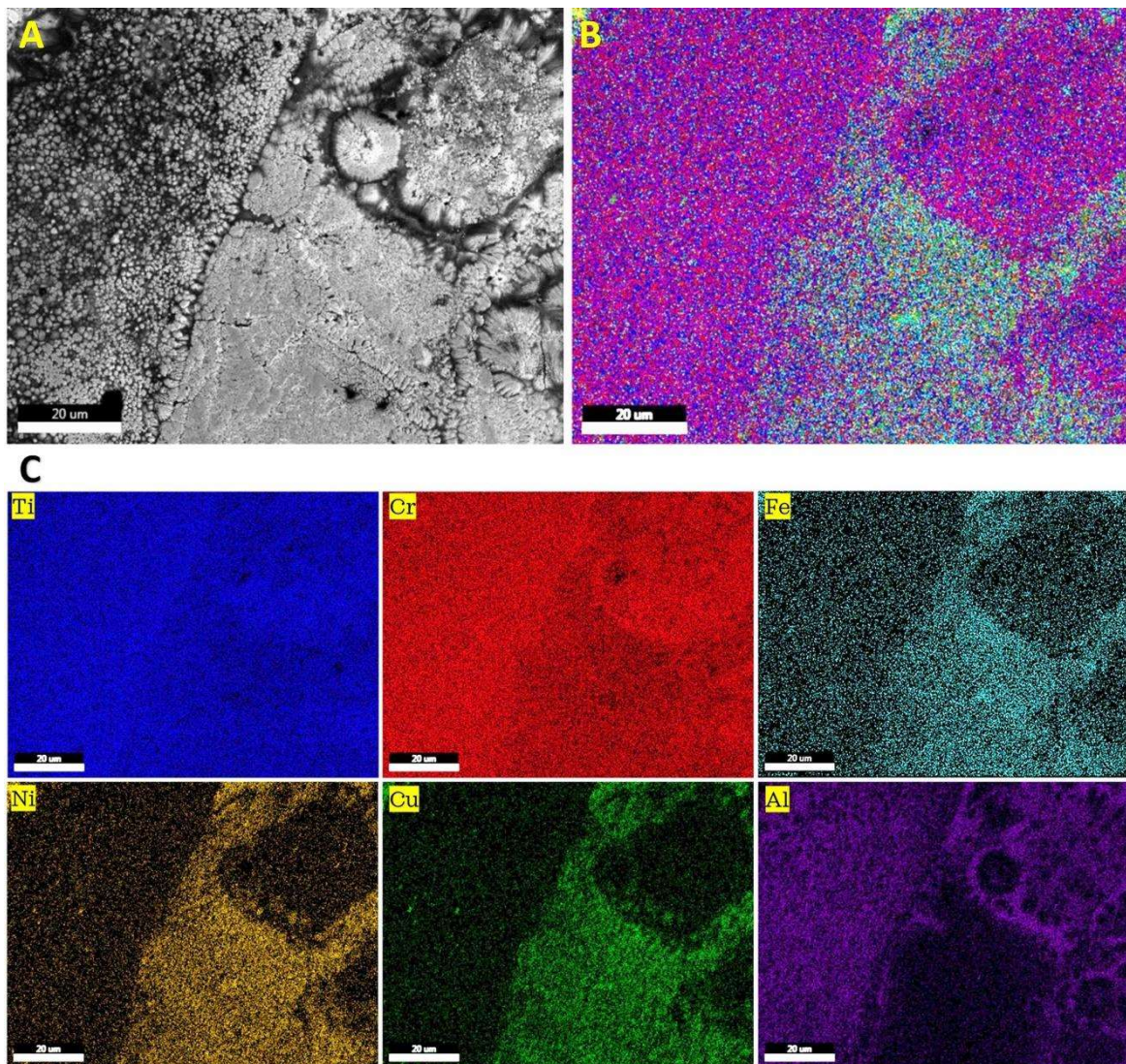


Figure 17: EDS mapping pictures of CuCrFeNiAl HEA in sample 2Y. (A) low magnification picture of sample surface, (B) distribution of all elements, & (C) individual element's distributions

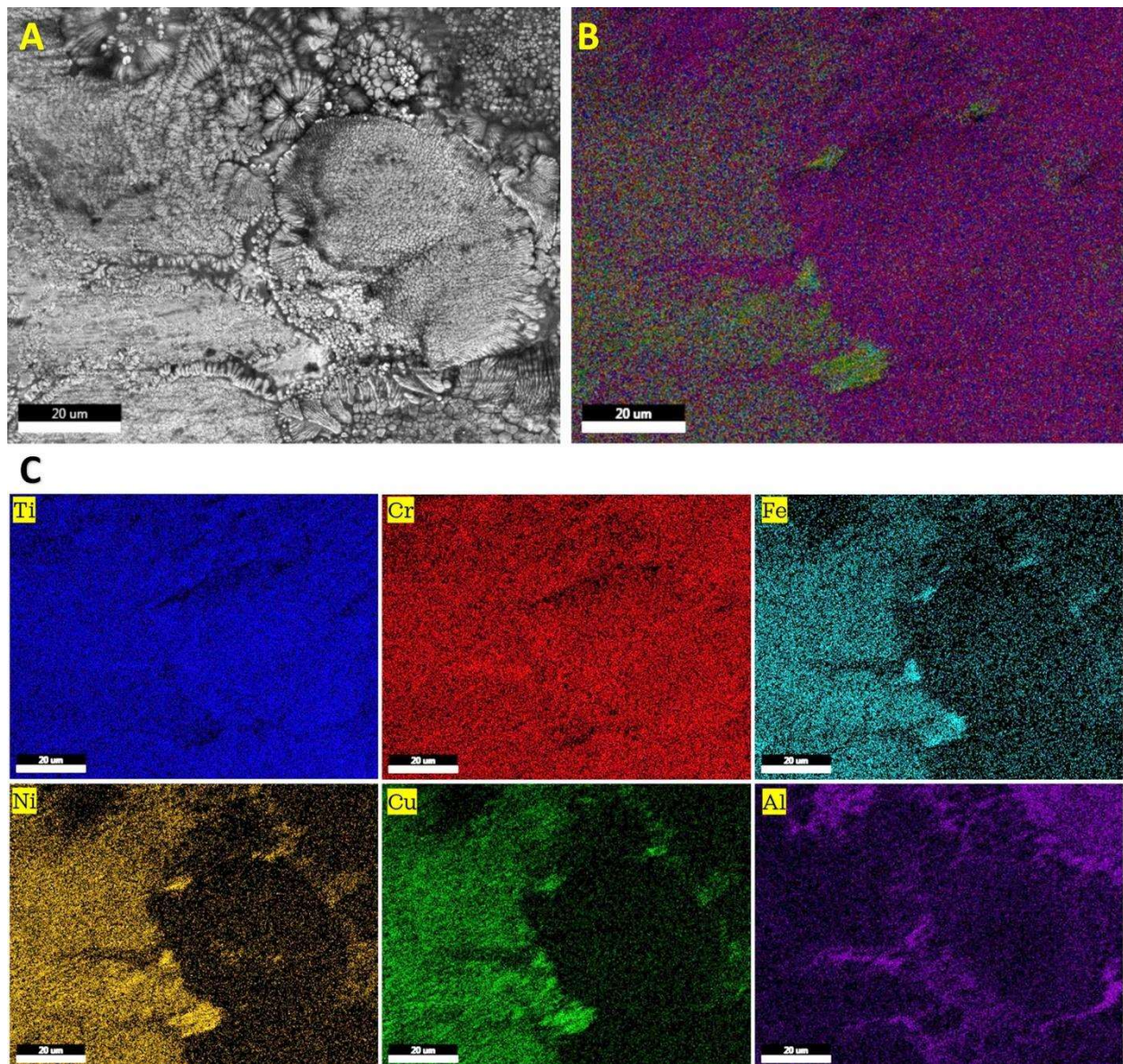


Figure 18: EDS mapping pictures of CuCrFeNiAl HEA in sample 2Z. (A) low magnification picture of sample surface, (B) distribution of all elements, & (C) individual element's distributions

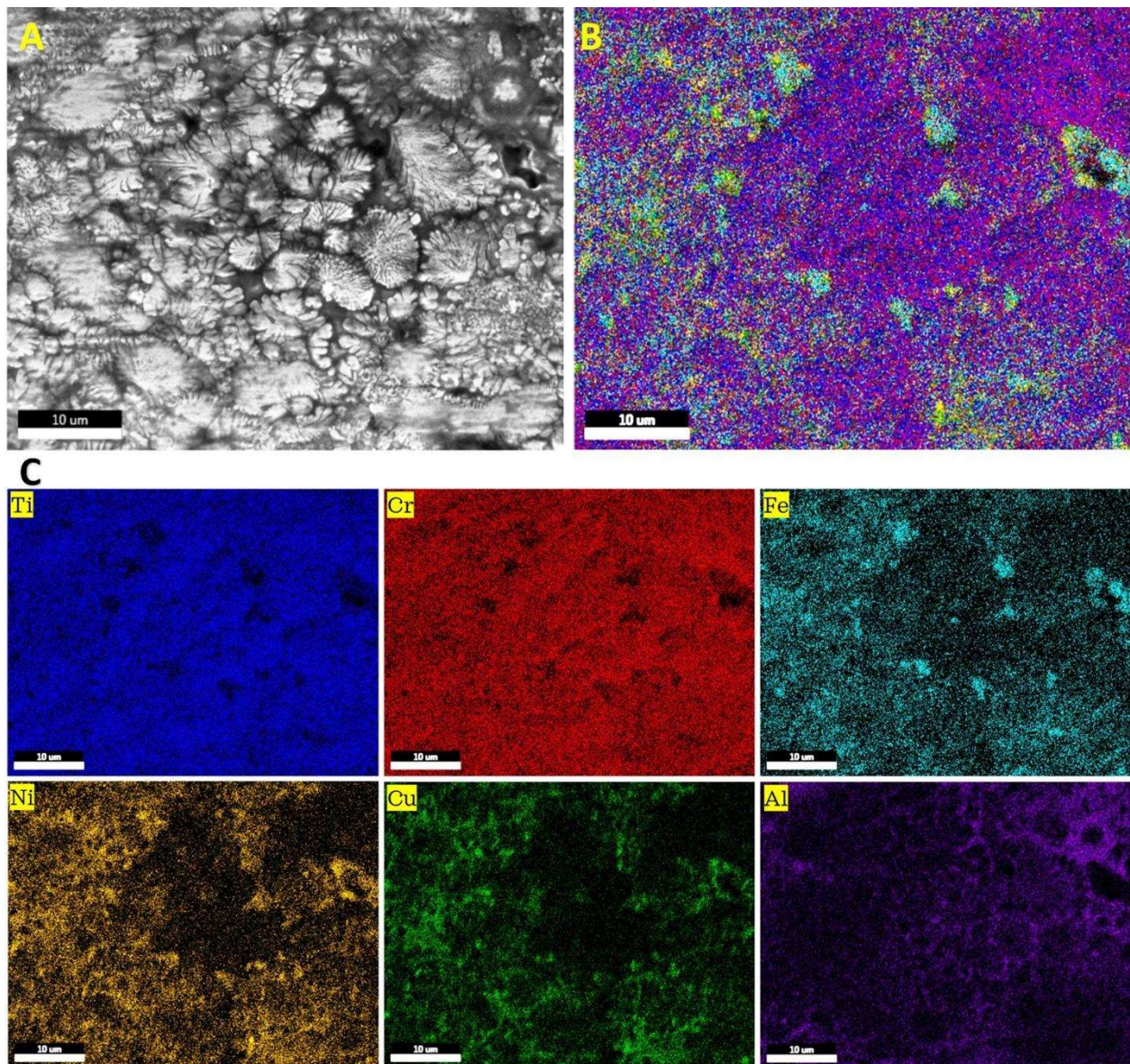


Figure 19: EDS mapping pictures of CuCrFeNiAl HEA in sample 2Y. (A) higher magnification picture of sample surface in dendritic area, (B) distribution of all elements, & (C) individual element's distributions

Table 8 shows the elemental distribution which is consistent with the eds mapping result. Fe, Ni and Cu were deposited in the dendritic area mostly. In the dendritic region, dendrites were rich of Ti and Cr while inter-dendrites were rich of Fe, Ni and Cu. Al were mostly distributed in

the petals and branches. Surprisingly, molar ratio of Al was very high in the branches. As branches were absence in the printed samples without Al, it can be assumed that the presence of Al was responsible for the creation of branches like structures.

Table 8: EDS of both samples

Sample	Phase	Ti	Cr	Fe	Ni	Cu	Al	Total
CuCrFeNiTiAl	dendrites	0.68	0.22	0.00	0.02	0.06	0.02	1.00
	petals	0.68	0.00	0.01	0.00	0.00	0.31	1.00
	small petals	0.45	0.30	0.00	0.00	0.00	0.25	1.00
	branches	0.20	0.00	0.00	0.00	0.00	0.80	1.00
CuCrFeNiTi		Ti	Cr	Fe	Ni	Cu	-	
	dendrites 1	0.57	0.00	0.02	0.19	0.22	-	1.00
	dendrites 2	0.58	0.00	0.03	0.17	0.22	-	1.00
	petals	0.35	0.02	0.07	0.27	0.29	-	1.00

4.3.3 Sample 2Y and 2Z of CuCrFeNiTi HEA

In the HEA sample without Al, Fe, Cr depleted from petals and dendrites as shown in Table 8. This can be explained by mixing enthalpies of principal elements calculated by the Miedema Approach [87](Table 9). Mixing enthalpies of binary eqioatomic alloys are listed in the table. From the table, Fe and Cr has the lowest negative mixing enthalpy, and these two elements have comparatively lower mixing enthalpy with other principal elements. That is why they depleted from other elements and petals and dendrites become rich of Ti, Ni and Cu.

Table 9: Mixing enthalpy of binary equiatomic alloys calculated by Miedema approach

Element	Cu	Cr	Fe	Ni	Ti	Al
Cu	-	12.5	12.9	3.6	-8.9	-7.6
Cr			-1.5	-6.7	-7.5	-9.9
Fe				-1.6	-16.8	-11.1
Ni					-34.5	-22.3
Ti						-29.5

4.4 Micro hardness of HEA Samples

Vickers hardness test was performed to measure the micro hardness of the as-built samples. The samples were grinded with 3 different diamond disks (220, 400 and 1200 grits) for 30 minutes. A force of 2.942 N was applied for each sample by a diamond shaped microhardness intender. Five readings were taken for a sample and then an average microhardness was measured. The result of the microhardness is given in Table 10.

Table 10: Micro-hardness of as-built CuCrFeNiTiAl and CuCrFeNiTi HEAs

Sample		1	2	3	4	5	Average Hardness (HV)
CuCrFeNiTiAl HEA	1A	661	679	779	758	737	722.8
	3C	779	737	779	802	758	771
	5E	851	802	877	851	826	841.4
CuCrFeNiTi HEA	2Y (1.5 mm scan)	720	720	705	752	769	733.2
	2Y (0.5 mm scan)	556	649	546	498	612	572.2
	2Z (1.5 mm scan)	786	803	803	803	636	766.2
	2Z (0.5 mm scan)	649	705	752	663	705	694.8

The average hardness of low, medium, and high energy density area samples was 722.8 HV, 771 HV, and 841.4 HV respectively in Vickers scale. In 5x5 test series, all the samples were printed with same scan length. The highest and the lowest scanning velocity were applied in the

highest energy density and the lowest energy density area samples respectively. In the highest energy density sample, laser moved faster to melt each subsequent track and facilitated higher temperature in the previously melted tracks. Thereby larger grains grew in the HEDA sample which reduced the total number of grains in this sample. According to Hall-Petch relation, hardness increases with decreasing grain size. Usually, grain boundary hinders the dislocation of grains. In case of refined grains, the grain boundary become larger which hinders the grain dislocation more effectively and more stress is required to dislocate or deform grains. Thereby with increasing energy density or decreasing scanning speed, hardness of printed materials increases. Hardness of the HEDA sample therefore got greater than other two samples.

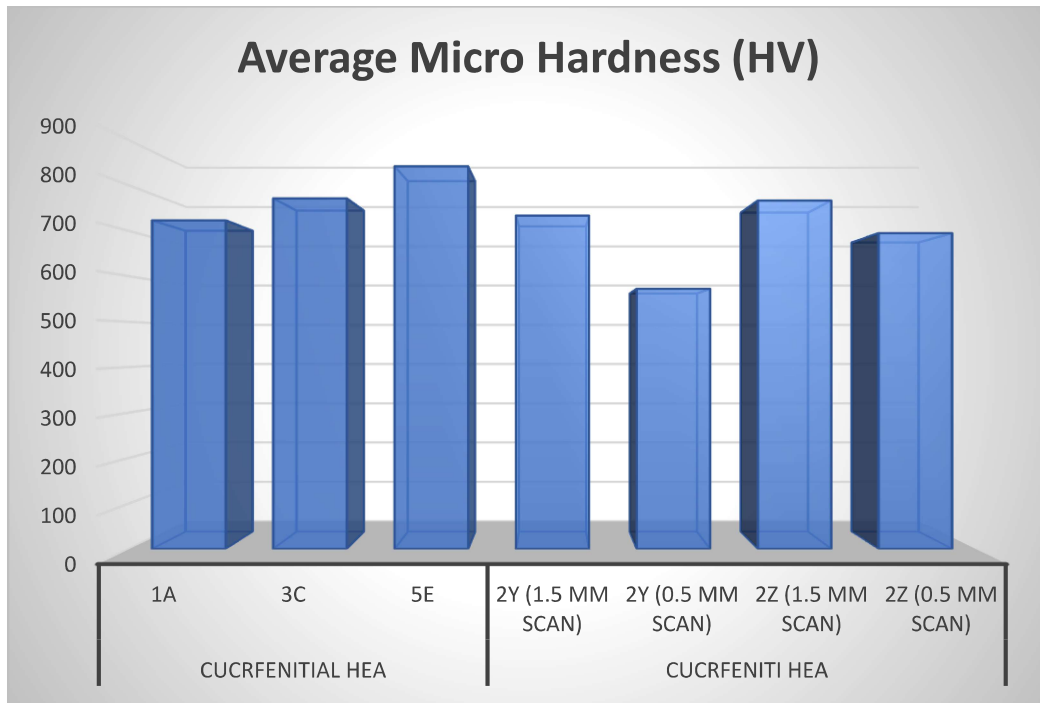


Figure 20: Average micro hardness of different CuCrFeNiTiAl HEA samples

In sample 2Z, for decreasing scan length from 1.5 mm to 0.5 mm, the hardness of the printed samples decreased from 766.2 HV to 694.8 HV. SEM pictures showed that the grains of the 0.5 mm sample were larger than that of 1.5 mm sample. Shorter scan length improved

heating in the subsequent tracks and therefore larger grains developed. The improved hardness in the shorter scan length sample is thereby can be explained by the Hall-Petch relation. Similarly, in sample 2Y, hardness of the lowest scan vector sample was 572.2 HV while a hardness of 733.2 HV is observed in the 1.5 mm sample. However, when hardness of the same scan length samples was compared, sample 2Z showed superior hardness property. As mentioned previously, for scanning a track in sample 2Z, laser takes twice the time needed to scan the same length in sample 2Y. Higher energy density made higher cooling rate in sample 2Z and resulted finer grains comparing to sample 2Y. Thereby, hardness of sample 2Z become greater than sample 2Y.

4.5 Surface Roughness of HEA Builds

Surface roughness of samples were measured using a Mahr GombH M300C surface roughness tester as shown in Figure 21. The results of the surface roughness test are provided in Table 11 and Figure 22 shows how surface quality of the samples changed due to different scanning strategies.

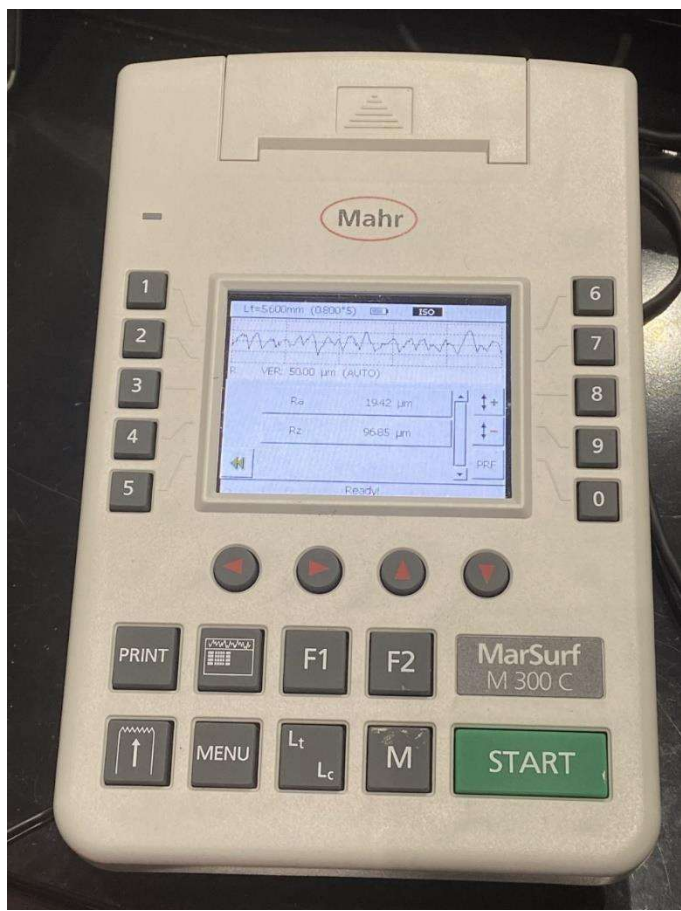


Figure 21: Mahr GombH M300C surface roughness testing device

The average roughness of 1.5 mm 2Y sample was found lower than that of 1.5 mm 2Z sample. This discrepancy can be explained by the Gaussian distribution of laser energy. According to this distribution, the intensity of laser power is the highest in the center of the laser beam and it gradually decreases to the boundary. As the laser moves very fast during the melting process, a large temperature gradient is created inside the track and the cooling rate varies in different areas of melt pool. The maximum cooling rate is found in the center and it decreases gradually from the center to the boundary. When the laser moves very rapidly, the melt pool becomes very thin, and it experiences very less variation in the thermal properties throughout the melt pool. When the scanning speed of the laser becomes slower, as the case in sample 2Z, the

melt pool becomes wider and thermal properties varies in the different area of the sample significantly. Therefore, 2Z sample has less stability in the melt pool comparing to the 2Y sample, and this phenomenon improved the surface quality in sample 2Y.

Table 11: Surface roughness of as-built CuCrFeNiTiAl and CuCrFeNiTi HEAs

Reading	1	2	3	4	5	Average Ra (μm)
2Y (1.5 mm scan)	17.68	18.4	17.13	16.4	17.06	17.334
2Y (0.5 mm scan)	17.56	17.28	16.15	16.94	17.11	17.008
2Z (1.5 mm scan)	19.42	18.22	18.41	17.78	18.87	18.54
2Z (0.5 mm scan)	17.78	18.52	17.52	17.39	16.65	17.572

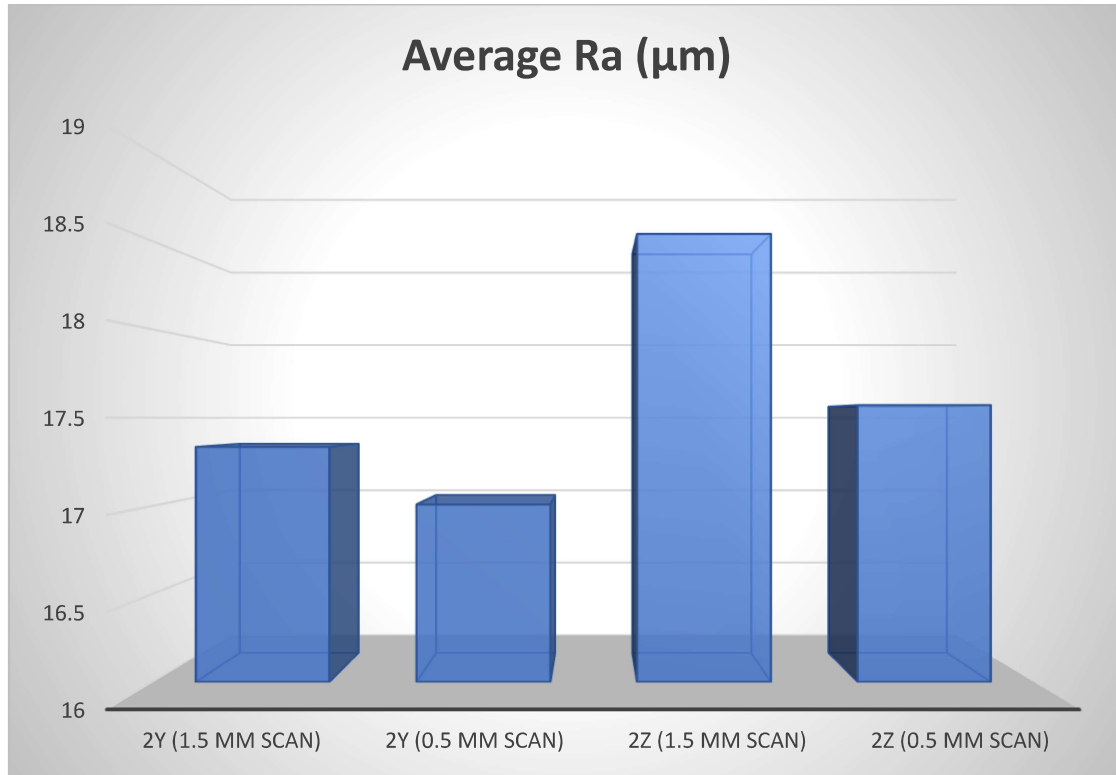


Figure 22: Average surface roughness of different CuCrFeNiTiAl HEA samples

Another reason behind the difference of surface finish between two same scan length samples is the development of porosities in the overlapping areas. Figure 23 shows the grinded surfaces of both samples. It is obvious that most of the porosities developed in the laser scanning direction. As both the samples has the same hatch distance, the rate of overlapping between two subsequent melt pools were the same. However, the scanning speed in sample 2Z was much slower than sample 2Y. In sample 2Z, due to the slower scanning speed, the laser took longer time to come back to melt the next track. Due to the rapid solidification in the SLM process, the previously melted track might have already dissipated most of the heat energy and the new track couldn't help the overlapping area to raise temperature to melting point as the laser intensity at the boundary of melt pools is much lower than the center. Thereby some of the powder in the overlapping area in the sample 2Z were not fully melted and lots of porosities appeared in the fabricated part. In case of sample 2Y, the laser scanning speed was double the speed in sample 2Z. So, the overlapping in sample 2Y could maintain comparatively higher temperature during the melting process. Stronger bonding among melt pools in sample 2Y reduced number of porosities and improved surface finish.

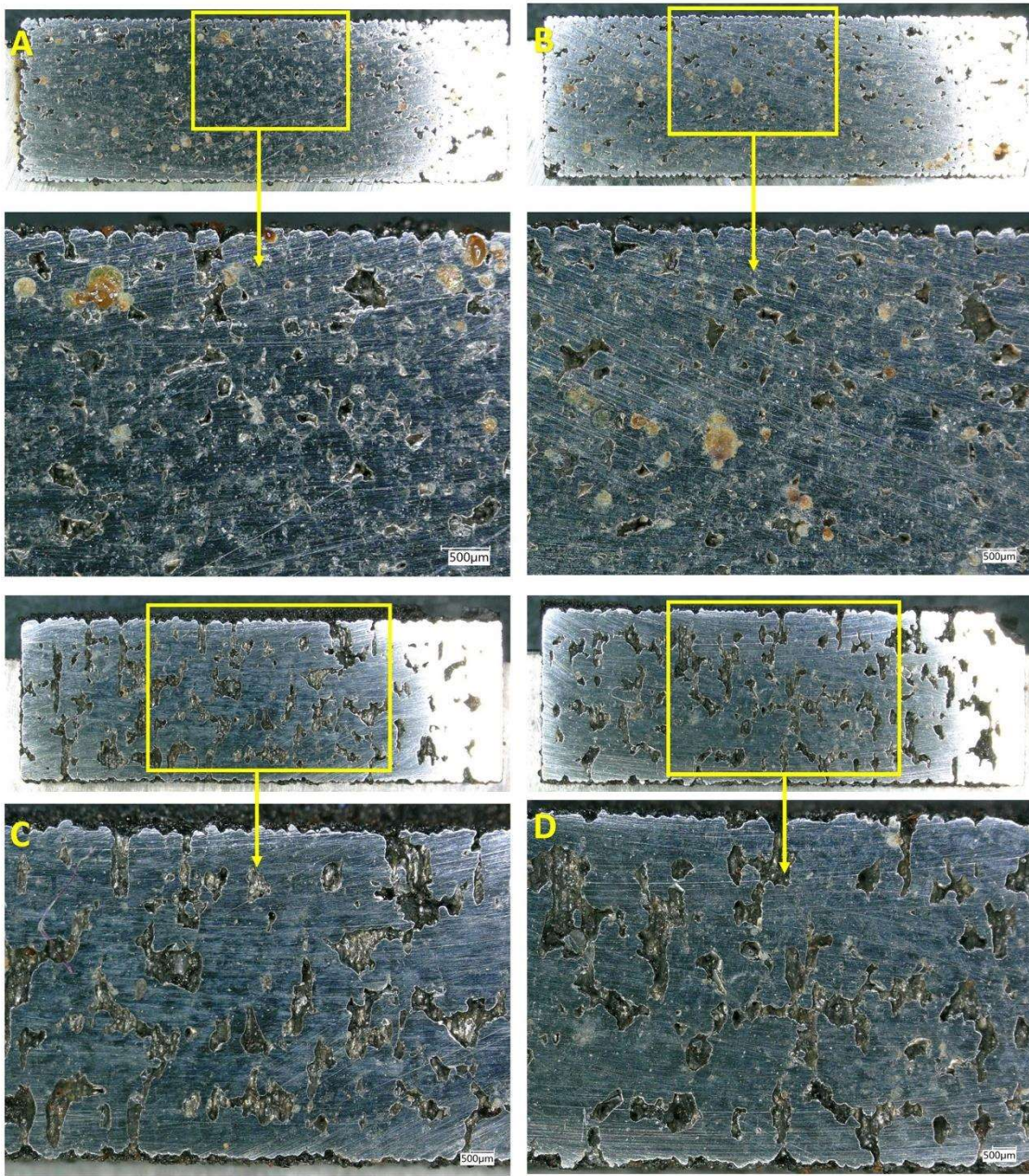


Figure 23: Surface roughness testing specimens of samples (A) 2Y0.5, (B) 2Y1.5, (C) 2Z0.5 & (D) 2Z1.5

When comparing different scan length samples with the same energy density, surface roughness in the lowest scan length sample was found comparatively better. In lower scan length sample, every new track helps maintain the temperature in the adjacent melt pool and thereby

decreases the temperature gradient in the melt pool. On the other hand, larger temperature gradient and resultant thermal properties variations happened in the larger scan length sample. Therefore, 0.5 mm sample showed better surface quality.

CHAPTER V

CONCLUSION

This study was intended to fabricate CuCrFeNiTiAl high entropy alloy by SLM process directly from the blend of six elemental powder materials. A sample 5X5 matrix was produced on a 50.8 mm × 50.8 mm customized stainless-steel substrate, using different laser power and scan speed via full factorial experimental design. Three representative samples were selected for analysis and comparison in the as-built status. To investigate the effect of variation in scan vector length on the melting and diffusion of HEA, two 3X3 test matrix were manufactured, one with Al and another without any Al content on the HEA system. Three samples from 3x3 test matrix were selected and from 5X5 test series, 2 samples were selected, and these selected samples were then characterized using XRD, to study crystal structures, and using SEM and EDX to study the microstructures and elemental composition respectively. Finally, surface roughness and micro-hardness of the samples were measured. The conclusions drawn based on the investigation can be summarized as below:

- (1) Mostly FCC and BCC crystal structures were observed in the SLM-fabricated CuCrFeNiTiAl and CuCrFeNiTi alloy samples with two strong peaks representing the structures appeared at 2θ between 42° and 45° . While XRD peaks in the CuCrFeNiTiAl HEA samples had higher intensities, comparatively lower intensities were observed in absence of Al in the alloy system. Besides, two peaks responsible for BCC structures emerged in the CuCrFeNiTi alloy at 2θ between 60° and 65° .

- (2) Through SEM observation at a low magnification, the samples exhibited non-uniform microstructural distribution which might be caused during the blending process.
- (3) At a high magnification of SEM, the microstructures in three samples appear fine-grained bright phases dispersed on dark phases. Shape, size and distribution of bright phases have a significant correlation with laser energy density under different printing parameters. The total area of bright phases increased with increasing energy input and the bright phases were most closely clustered in high energy density sample.
- (4) In 3X3 test series, four different grain morphologies were observed such as dendrites, rosette, petals, and branches. With decreasing the laser scan vector lengths, the average sizes of the grains increased. It indicates that in case of shorter scan vectors, new scan tracks helped the previously melted track to keep high temperature and thereby facilitated the slower cooling of the melt pool.
- (5) Although the 2Y samples were printed at lower energy density, growth of grains of these samples were better than the highest energy density 2Z samples. In 2Y sample, higher number of dendrites developed with an average size of 3-6 μm . The reason behind this might be the comparative higher laser scan velocity. However, a significant number of porosities were observed in the 2Y sample at the overlaps.
- (6) While all the SLM fabricated CuCrFeNiTiNiAl alloys showed stripes structures in the overlapping area, exclusion of Al in the alloy system generated build surface without any borders between the melt pool and the overlapping area. There were also no branches type structures found in the CuCrFeNiTiNi alloy.
- (7) Though mixed in equimolar ratio, no equal compositions of the five principal elements were obtained based on EDX results, indicating incomplete diffusion during melting and

solidification process. Overall, Ti and Cr had a better distribution in the printed alloys. However, they were found segregated in the dendritic areas in the CuCrFeNiTiNiAl samples. In the CuCrFeNiTiNi alloy, Fe and Cr depleted from the petals and dendrites due to their lower mixing enthalpy.

- (8) Micro-hardness of the samples was found have a correlation with energy density. With the increasing energy input, micro-hardness of the samples also increased. Again, micro-hardness of the samples decreased with shorter scan vector as shorter scans helped development of larger grains.
- (9) Laser scan vector lengths had a direct impact on the surface quality of the samples. Surface roughness of the builds were found comparatively improved when a shorter scan vector was used.

REFERENCES

- [1] Zhang, Y., et al., *Microstructures and properties of high-entropy alloys*. Progress in Materials Science, 2014. 61: p. 1-93.
- [2] Tsai, M.-H. and J.-W. Yeh, *High-entropy alloys: a critical review*. Materials Research Letters, 2014. 2(3): p. 107-123.
- [3] Cantor, B., et al., *Microstructural development in equiatomic multicomponent alloys*. Materials Science and Engineering: A, 2004. 375: p. 213-218.
- [4] Yeh, J.W., et al., *Nanostructured high-entropy alloys with multiple principal elements: novel alloy design concepts and outcomes*. Advanced Engineering Materials, 2004. 6(5): p. 299-303.
- [5] Jien-Wei, Y., *Recent progress in high entropy alloys*. Ann. Chim. Sci. Mat, 2006. 31(6): p. 633-648.
- [6] Tong, C.-J., et al., *Mechanical performance of the Al x CoCrCuFeNi high-entropy alloy system with multiprincipal elements*. Metallurgical and Materials Transactions A, 2005. 36(5): p. 1263-1271.
- [7] Wen, L., et al., *Effect of aging temperature on microstructure and properties of AlCoCrCuFeNi high-entropy alloy*. Intermetallics, 2009. 17(4): p. 266-269.
- [8] Singh, S., et al., *Decomposition in multi-component AlCoCrCuFeNi high-entropy alloy*. Acta Materialia, 2011. 59(1): p. 182-190.
- [9] Tsai, M.-H., et al., *Morphology, structure and composition of precipitates in Al0. 3CoCrCu0. 5FeNi high-entropy alloy*. Intermetallics, 2013. 32: p. 329-336.
- [10] Li, C., et al., *Effect of aluminum contents on microstructure and properties of AlxCoCrFeNi alloys*. Journal of Alloys and Compounds, 2010. 504: p. S515-S518.
- [11] Wang, W.-R., et al., *Effects of Al addition on the microstructure and mechanical property of AlxCoCrFeNi high-entropy alloys*. Intermetallics, 2012. 26: p. 44-51.
- [12] Chen, M.-R., et al., *Microstructure and properties of Al0. 5CoCrCuFeNiTix (x= 0-2.0) high-entropy alloys*. Materials Transactions, 2006. 47(5): p. 1395-1401.
- [13] Zhou, Y., et al., *Solid solution alloys of Al Co Cr Fe Ni Ti x with excellent room-temperature mechanical properties*. Applied physics letters, 2007. 90(18): p. 181904.
- [14] Zhao, Y., et al., *A hexagonal close-packed high-entropy alloy: The effect of entropy*. Materials & Design, 2016. 96: p. 10-15.

- [15] Couzinié, J., et al., *Microstructure of a near-equimolar refractory high-entropy alloy*. Materials Letters, 2014. 126: p. 285-287.
- [16] Zhang, K., et al., *Microstructure and mechanical properties of CoCrFeNiTiAl_x high-entropy alloys*. Materials Science and Engineering: A, 2009. 508(1-2): p. 214-219.
- [17] Gild, J., et al., *High-entropy metal diborides: a new class of high-entropy materials and a new type of ultrahigh temperature ceramics*. Scientific reports, 2016. 6: p. 37946.
- [18] Yeh, J.-W., et al., *Anomalous decrease in X-ray diffraction intensities of Cu–Ni–Al–Co–Cr–Fe–Si alloy systems with multi-principal elements*. Materials chemistry and physics, 2007. 103(1): p. 41-46.
- [19] Liverani, E., et al., *Effect of selective laser melting (SLM) process parameters on microstructure and mechanical properties of 316L austenitic stainless steel*. Journal of Materials Processing Technology, 2017. 249: p. 255-263.
- [20] Tsai, K.-Y., M.-H. Tsai, and J.-W. Yeh, *Sluggish diffusion in Co–Cr–Fe–Mn–Ni high-entropy alloys*. Acta Materialia, 2013. 61(13): p. 4887-4897.
- [21] Vaidya, M., et al., *Ni tracer diffusion in CoCrFeNi and CoCrFeMnNi high entropy alloys*. Journal of Alloys and Compounds, 2016. 688: p. 994-1001.
- [22] Wang, Y., et al., *Microstructure and compressive properties of AlCrFeCoNi high entropy alloy*. Materials Science and Engineering: A, 2008. 491(1-2): p. 154-158.
- [23] Zhu, J.M., et al., *Microstructures and compressive properties of multicomponent AlCoCrFeNiMo_x alloys*. Materials Science & Engineering: A (Structural Materials: Properties, Microstructure and Processing), 2010. 527(26): p. 6975-9.
- [24] Gorr, B., et al., *Phase equilibria, microstructure, and high temperature oxidation resistance of novel refractory high-entropy alloys*. Journal of Alloys and Compounds, 2015. 624: p. 270-278.
- [25] Hsu, C.-Y., et al., *Effect of iron content on wear behavior of AlCoCrFexMo0.5Ni high-entropy alloys*. Wear, 2010. 268(5): p. 653-659.
- [26] Chen, P., et al., *Fabricating CoCrFeMnNi high entropy alloy via selective laser melting in-situ alloying*. Journal of Materials Science and Technology, 2020. 43: p. 40-43.
- [27] Li, N., et al., *Fe-based metallic glass reinforced FeCoCrNiMn high entropy alloy through selective laser melting*. Journal of Alloys and Compounds, 2020. 822.
- [28] Tonelli, L., et al., *Effects of powders and process parameters on density and hardness of A357 aluminum alloy fabricated by selective laser melting*. International Journal of Advanced Manufacturing Technology, 2020. 106(1-2): p. 371-383.
- [29] Tonelli, L., A. Fortunato, and L. Ceschini, *CoCr alloy processed by selective laser melting (SLM): Effect of laser energy density on microstructure, surface morphology, and hardness*. Journal of Manufacturing Processes, 2020. 52: p. 106-119.

- [30] Zhou, R., et al., *Microstructures and mechanical properties of C-containing FeCoCrNi high-entropy alloy fabricated by selective laser melting*. Intermetallics, 2018. 94: p. 165-171.
- [31] Luo, S., et al., *Selective laser melting of an equiatomic AlCrCuFeNi high-entropy alloy: Processability, non-equilibrium microstructure and mechanical behavior*. Journal of Alloys and Compounds, 2019. 771: p. 387-397.
- [32] Guo, L., et al., *Effects of elemental segregation and scanning strategy on the mechanical properties and hot cracking of a selective laser melted FeCoCrNiMn-(N, Si) high entropy alloy*. Journal of Alloys and Compounds, 2021. 865: p. 158892.
- [33] Kim, Y.-K., et al., *In-situ formed oxide enables extraordinary high-cycle fatigue resistance in additively manufactured CoCrFeMnNi high-entropy alloy*. Additive Manufacturing, 2021. 38: p. 101832.
- [34] Litwa, P., et al., *The additive manufacture processing and machinability of CrMnFeCoNi high entropy alloy*. Materials & Design, 2021. 198: p. 109380.
- [35] Guo, S., *Phase selection rules for cast high entropy alloys: an overview*. Materials Science and Technology, 2015. 31(10): p. 1223-1230.
- [36] Guo, S., C. Ng, and C.T. Liu, *Anomalous solidification microstructures in Co-free Al_xCrCuFeNi₂ high-entropy alloys*. Journal of alloys and compounds, 2013. 557: p. 77-81.
- [37] Ng, C., et al., *Phase stability and tensile properties of Co-free Al0. 5CrCuFeNi2 high-entropy alloys*. Journal of alloys and compounds, 2014. 584: p. 530-537.
- [38] Liu, L., et al., *Microstructure and the properties of FeCoCuNiSn_x high entropy alloys*. Materials Science and Engineering: A, 2012. 548: p. 64-68.
- [39] Senkov, O., et al., *Refractory high-entropy alloys*. Intermetallics, 2010. 18(9): p. 1758-1765.
- [40] Yang, X., Y. Zhang, and P. Liaw, *Microstructure and compressive properties of NbTiVTaAl_x high entropy alloys*. Procedia Engineering, 2012. 36: p. 292-298.
- [41] Zhang, Z., E.-H. Han, and C. Xiang, *Irradiation behaviors of two novel single-phase bcc-structure high-entropy alloys for accident-tolerant fuel cladding*. Journal of Materials Science & Technology, 2021. 84: p. 230-238.
- [42] Feuerbacher, M., M. Heidelmann, and C. Thomas, *Hexagonal high-entropy alloys*. Materials Research Letters, 2015. 3(1): p. 1-6.
- [43] Takeuchi, A., et al., *High-entropy alloys with a hexagonal close-packed structure designed by equi-atomic alloy strategy and binary phase diagrams*. Jom, 2014. 66(10): p. 1984-1992.
- [44] Youssef, K. and S.R. Roberto, *Applications of salt solutions before and after harvest affect the quality and incidence of postharvest gray mold of 'Italia' table grapes*. Postharvest Biology and Technology, 2014. 87: p. 95-102.

- [45] Lin, C.-M. and H.-L. Tsai, *Evolution of microstructure, hardness, and corrosion properties of high-entropy Al0. 5CoCrFeNi alloy*. Intermetallics, 2011. 19(3): p. 288-294.
- [46] Hsu, C.-Y., et al., *Effect of iron content on wear behavior of AlCoCrFexMo0. 5Ni high-entropy alloys*. Wear, 2010. 268(5-6): p. 653-659.
- [47] Zhu, J., et al., *Microstructures and compressive properties of multicomponent AlCoCrCuFeNiMox alloys*. Journal of alloys and compounds, 2010. 497(1-2): p. 52-56.
- [48] Chuang, M.-H., et al., *Microstructure and wear behavior of AlxCo1. 5CrFeNi1. 5Tiy high-entropy alloys*. Acta Materialia, 2011. 59(16): p. 6308-6317.
- [49] Wu, J.-M., et al., *Adhesive wear behavior of AlxCoCrCuFeNi high-entropy alloys as a function of aluminum content*. Wear, 2006. 261(5-6): p. 513-519.
- [50] Chen, M.-R., et al., *Effect of vanadium addition on the microstructure, hardness, and wear resistance of Al 0.5 CoCrCuFeNi high-entropy alloy*. Metallurgical and Materials Transactions A, 2006. 37(5): p. 1363-1369.
- [51] Hemphill, M.A., et al., *Fatigue behavior of Al0. 5CoCrCuFeNi high entropy alloys*. Acta Materialia, 2012. 60(16): p. 5723-5734.
- [52] Chen, Y., et al., *Microstructure and electrochemical properties of high entropy alloys—a comparison with type-304 stainless steel*. Corrosion science, 2005. 47(9): p. 2257-2279.
- [53] Hsu, Y.-J., W.-C. Chiang, and J.-K. Wu, *Corrosion behavior of FeCoNiCrCux high-entropy alloys in 3.5% sodium chloride solution*. Materials Chemistry and Physics, 2005. 92(1): p. 112-117.
- [54] Lee, C., et al., *The effect of boron on the corrosion resistance of the high entropy alloys Al0. 5CoCrCuFeNiB x*. Journal of the Electrochemical Society, 2007. 154(8): p. C424-C430.
- [55] Hsu, C.-Y., et al., *On the superior hot hardness and softening resistance of AlCoCr_xFeMo0. 5Ni high-entropy alloys*. Materials Science and Engineering: A, 2011. 528(10-11): p. 3581-3588.
- [56] Senkov, O.N., et al., *Mechanical properties of Nb25Mo25Ta25W25 and V20Nb20Mo20Ta20W20 refractory high entropy alloys*. Intermetallics, 2011. 19(5): p. 698-706.
- [57] Jang, M.J., et al., *High-temperature tensile deformation behavior of hot rolled CrMnFeCoNi high-entropy alloy*. Journal of Alloys and Compounds, 2018. 730: p. 242-248.
- [58] Licavoli, J.J., et al., *Microstructure and mechanical behavior of high-entropy alloys*. Journal of Materials Engineering and Performance, 2015. 24(10): p. 3685-3698.
- [59] Sourav, A., S. Yebaji, and S. Thangaraju, *Structure-property relationships in hot forged AlxCoCrFeNi high entropy alloys*. Materials Science and Engineering: A, 2020. 793: p. 139877.

- [60] Chen, H., et al., *Improving additive manufacturing processability of hard-to-process overhanging structure by selective laser melting*. Journal of Materials Processing Technology, 2017. 250: p. 99-108.
- [61] Attar, H., et al., *Selective laser melting of in situ titanium–titanium boride composites: processing, microstructure and mechanical properties*. Acta Materialia, 2014. 76: p. 13-22.
- [62] Attar, H., et al., *Nanoindentation and wear properties of Ti and Ti-TiB composite materials produced by selective laser melting*. Materials Science and Engineering: A, 2017. 688: p. 20-26.
- [63] Gu, D.D., et al., *Laser additive manufacturing of metallic components: materials, processes and mechanisms*. International materials reviews, 2012. 57(3): p. 133-164.
- [64] Rao, H., et al., *The influence of processing parameters on aluminium alloy A357 manufactured by Selective Laser Melting*. Materials & Design, 2016. 109: p. 334-346.
- [65] Zhou, L., et al., *Selective laser melting of pure tantalum: densification, microstructure and mechanical behaviors*. Materials Science and Engineering: A, 2017. 707: p. 443-451.
- [66] Huang, Y., et al., *Finite element analysis of thermal behavior of metal powder during selective laser melting*. International Journal of Thermal Sciences, 2016. 104: p. 146-157.
- [67] He, K. and X. Zhao, *3D thermal finite element analysis of the SLM 316L parts with microstructural correlations*. Complexity, 2018. 2018.
- [68] Kruth, J.-P., et al., *Selective laser melting of iron-based powder*. Journal of materials processing technology, 2004. 149(1-3): p. 616-622.
- [69] Lu, Y., et al., *Study on the microstructure, mechanical property and residual stress of SLM Inconel-718 alloy manufactured by differing island scanning strategy*. Optics & Laser Technology, 2015. 75: p. 197-206.
- [70] Xiong, W., et al., *Effect of selective laser melting parameters on morphology, microstructure, densification and mechanical properties of supersaturated silver alloy*. Materials & Design, 2019. 170: p. 107697.
- [71] Jia, H., et al., *Scanning strategy in selective laser melting (SLM): a review*. The International Journal of Advanced Manufacturing Technology, 2021: p. 1-23.
- [72] Ramos, D., F. Belblidia, and J. Sienz, *New scanning strategy to reduce warpage in additive manufacturing*. Additive Manufacturing, 2019. 28: p. 554-564.
- [73] Zou, S., et al., *Numerical analysis of the effect of the scan strategy on the residual stress in the multi-laser selective laser melting*. Results in Physics, 2020. 16: p. 103005.
- [74] Wang, L., et al., *An approach to predict the residual stress and distortion during the selective laser melting of AlSi10Mg parts*. The International Journal of Advanced Manufacturing Technology, 2018. 97(9-12): p. 3535-3546.

- [75] AlMangour, B., D. Grzesiak, and J.-M. Yang, *Scanning strategies for texture and anisotropy tailoring during selective laser melting of TiC/316L stainless steel nanocomposites*. Journal of Alloys and Compounds, 2017. 728: p. 424-435.
- [76] Thijs, L., et al., *Fine-structured aluminium products with controllable texture by selective laser melting of pre-alloyed AlSi10Mg powder*. Acta Materialia, 2013. 61(5): p. 1809-1819.
- [77] Trosch, T., et al., *Microstructure and mechanical properties of selective laser melted Inconel 718 compared to forging and casting*. Materials letters, 2016. 164: p. 428-431.
- [78] Dong, Z., et al., *Effect of hatch spacing on melt pool and as-built quality during selective laser melting of stainless steel: Modeling and experimental approaches*. Materials, 2019. 12(1): p. 50.
- [79] Sateesh, N., et al., *Microstructure and mechanical characterization of laser sintered Inconel-625 superalloy*. Procedia Materials Science, 2014. 5: p. 772-779.
- [80] Carter, L.N., et al., *The influence of the laser scan strategy on grain structure and cracking behaviour in SLM powder-bed fabricated nickel superalloy*. Journal of Alloys and Compounds, 2014. 615: p. 338-347.
- [81] Pupo, Y., et al., *Scanning space analysis in selective laser melting for CoCrMo powder*. Procedia Engineering, 2013. 63: p. 370-378.
- [82] Aboulkhair, N.T., et al., *Reducing porosity in AlSi10Mg parts processed by selective laser melting*. Additive manufacturing, 2014. 1: p. 77-86.
- [83] Promoppatum, P. and S.-C. Yao, *Influence of scanning length and energy input on residual stress reduction in metal additive manufacturing: Numerical and experimental studies*. Journal of Manufacturing Processes, 2020. 49: p. 247-259.
- [84] Gibson, I., D.W. Rosen, and B. Stucker, *Additive manufacturing technologies*. Vol. 17. 2014: Springer.
- [85] Cryosystems, O., *Crystallographica search-match*. Journal of Applied Crystallography, 1999. 32(2): p. 379-380.
- [86] Easton, M., C. Davidson, and D. StJohn, *Grain morphology of as-cast wrought aluminium alloys*. Materials transactions, 2011. 52(5): p. 842-847.
- [87] Takeuchi, A. and A. Inoue, *Mixing enthalpy of liquid phase calculated by Miedema's scheme and approximated with sub-regular solution model for assessing forming ability of amorphous and glassy alloys*. Intermetallics, 2010. 18(9): p. 1779-1789.

BIOGRAPHICAL SKETCH

Joni Chandra Dhar has acquired his bachelor's degree in Industrial and Production Engineering from Shahjalal University of Science and Technology in 2016 and joined the department of Manufacturing and Industrial Engineering at the University of Texas Rio Grande Valley in Fall 2019 for pursuing a Master's. He worked as a research assistant at the Additive Manufacturing lab under Dr. Jianzhi Li and completed his Master of Science in Manufacturing Engineering in August 2021. His research interests are focused additive manufacturing, and high entropy alloys. During his Master's, he was awarded the Presidential Graduate Research Assistantship award for all two years. He has submitted one article in a prestigious journal, one poster presentation, and is on the verge of submitting another article. For pursuing a Ph.D. degree, he is expected to join the Rensselaer Polytechnic University, Troy, New York in the Mechanical, Aerospace and Nuclear Engineering department. He can be reached at joni.c.dhar@gmail.com.

ProQuest Number: 28647651

INFORMATION TO ALL USERS

The quality and completeness of this reproduction is dependent on the quality
and completeness of the copy made available to ProQuest.



Distributed by ProQuest LLC (2021).

Copyright of the Dissertation is held by the Author unless otherwise noted.

This work may be used in accordance with the terms of the Creative Commons license or other rights statement, as indicated in the copyright statement or in the metadata associated with this work. Unless otherwise specified in the copyright statement or the metadata, all rights are reserved by the copyright holder.

This work is protected against unauthorized copying under Title 17,
United States Code and other applicable copyright laws.

Microform Edition where available © ProQuest LLC. No reproduction or digitization of the Microform Edition is authorized without permission of ProQuest LLC.

ProQuest LLC
789 East Eisenhower Parkway
P.O. Box 1346
Ann Arbor, MI 48106 - 1346 USA